# FE modeling of concrete with strong discontinuities for 3D shear fractures and comparison with experimental results

Yue Sun, Emmanuel Roubin, Jianfu Shao, Jean-Baptiste Colliat

# FE modeling of concrete with strong discontinuities for 3D shear fractures and comparison with experimental results

Yue SUN[a], Emmanuel ROUBIN[b], Jianfu SHAO[a] and Jean-Baptiste COLLIAT[a]

[a]Laboratoire de Mécanique, Multiphysique, Multiéchelle (LaMcube), University of Lille, Centrale Lille, CNRS, Lille, France
[b]Université Grenoble Alpes, CNRS, Grenoble INP, 3SR, Grenoble F-38000, France

ARTICLE INFO

*Keywords*:
E-FEM method
Heterogeneous quasi-brittle materials
Frictional sliding fractures
Crack closure mechanism

ABSTRACT

In this paper, a new Enhanced Finite Element Method (E-FEM) model is proposed to describe 3D shear fractures of quasi-brittle materials such as concrete. Special attention is made to the failure behaviors in cyclic loadings as it is a common phenomenon in practical engineering. Within the framework of the E-FEM, the discontinuities are locally embedded in the finite elements. Here, two kinds of discontinuity enhancements are used in this model: weak discontinuities allow the model to represent heterogeneities in an unstructured mesh explicitly, and strong discontinuities enable the displacement jumps in finite elements to perform cracks and fractures. In this paper, our interest is focused on the shear sliding discontinuity (mode-II). The closure mechanism is also taken into concern, which simulates frictional sliding forward and backward between the lips of cracks. Then the performance of the proposed model is tested and analyzed by comparing it to experimental results. Certain limitations of the simulation are pointed out, and the corresponding solutions are addressed. Finally, the consistencies and differences between the simulation and the experimental results are discussed.

## 1. Introduction

Over the last few decades, multiple studies have been carried out to describe and model failure behaviors of quasi-brittle materials such as concrete. Among several mechanical responses of these materials, failure behaviors under cyclic compressive loadings have attracted particular attention because of their complexity and important role in civil engineering structures. Naturally, the macroscopic behaviors are known a priori from experimental tests. Various computational models have been proposed to reproduce experimental observations referred to as the macroscopic models or the phenomenological models. The degradation of the material is governed by laws that are defined over the global specimen, such as damage models (Mazars, 1984; Kupfer, Hilsdorf and Rusch, 1969; Yang, Dong, Liu, Yi and He, 2018) and the plasticity theories (Chen and Chen, 1975; Dragon and Mroz, 1979; Hofstetter and Mang, 1995), just mention a few. A lot of them achieved at reproducing many typical behaviors of brittle/quasi-brittle materials by enriching the model with the addition of crack closure (Comi and Perego, 2001; Wosatko, Genikomsou, Pamin, Polak and Winnicki, 2018), associating the damage with the number of cycles (T.C. Hsu, 1981; Ramakrishnan and Malhotra, 1993), proposing thermodynamics with irreversible processes (Alliche, 2004; Ragueneau, 2007), or coupling the damage with the friction or the plasticity (Desmorat, Ragueneau and Pham, 2007).

Macroscopic models are well adapted to perform simulations for structures such as bridges and dams. However, the description of complex material behaviors requires growing complicated governing laws and specific parameters, and the physical resources of fractures may not be explicitly explained. Additionally, such models usually suffer from the mesh-dependence and spurious stress locking (Rots, Nauta, Kuster and Blaauwendraad, 1985; Jirasek and Zimmermann, 1998), which requires advanced techniques such as the non-local models and gradient-enhanced models (Pijaudier-Cabot and Bažant, 1987; Peerlings, De Borst, Brekelmans and Geers, 1998; Pandolfi, Krysl and Ortiz, 1999; Bažant and Jirásek, 2002). In general, it is accepted that the complex macroscopic behaviors of such heterogeneous material may take their origin at smaller scales such as the micro or meso-scale. At these scales, the initiation and propagation of micro-cracks are strongly influenced by the heterogeneous structures of material such as the hard inclusions and macro-pores. Aiming at simulating explicit cracks and heterogeneities, the method used in this paper is based on the discontinuity approach, namely the Enhanced Finite Element Method (E-FEM) (Ortiz, Leroy and Needleman, 1987; Simo, Oliver and Armero, 1993).

ORCID(s):

In the context of enriched Finite Element Methods, E-FEM is an element-enriched method that the additional degree of freedom is attached to the element. In many cases, the enrichment can be considered as element-wise local variables, and can be eliminated at the element level by static condensation. By taking advantage of this strategy, the size of the solving system is constant no matter how many cracks are initiated in the solid. In this paper, two kinds of enhancement are considered: i) the strong discontinuity (Simo et al., 1993; Wells, 2001) is used to simulate cracks and localization at the meso-scale; ii) the weak discontinuity (Ortiz et al., 1987; Sukumar, Chopp, Moës and Belytschko, 2001) is embedded in the element to represent explicit heterogeneity interfaces, which provides high-quality mesh result even for complex geometry by using the non-adapted mesh strategy (Moës, Cloirec, Cartraud and Remacle, 2003). By combining the weak and strong discontinuities in the same finite element, the model is capable of simulating complex crack patterns such as the debonding on the heterogeneity interfaces and branching of multi-cracks (Benkemoun, Hautefeuille, Colliat and Ibrahimbegovic, 2010).

In existing E-FEM models, many enriched modes have been proposed to the discontinuity (Roubin, Vallade, Benkemoun and Colliat, 2015; Hauseux, Roubin, Seyedi and Colliat, 2016) to simulate different behaviors of material such as the progressive loss of stiffness and asymmetric tension/compression softening. In this paper, the focus is made on the mode-II discontinuities, which stands for the frictional sliding-opening between the cracks. Following the study developed in Hauseux (2015) and Vallade (2016), we add firstly weak discontinuities in the model to concern the heterogeneity interfaces. Then our attention is mainly focused on the mechanism of crack closure, which, in the context of mode-II discontinuity, stands for the sliding "backward" between the lips of cracks. Considering the friction between the lips of crack, but no plasticity or hardening function is implemented in the model, it would be interesting to analyze the behavior of the material under cyclic loading, and investigate the necessary mechanism causing the hysteresis effect of the materials.

This paper is organized in the following way. In Section 2, a brief overview of the kinematical enhancements is presented. Here, our interest is made on mode-II cracks. Then in Section 3, the governing equations for the mechanical kinematics on the discrete discontinuity surface are addressed. The closure mechanism, which is our key contribution, is also detailed in this section. Section 4 presents the formulation of the Finite Element approximation and the resolution strategy. Next, as a first step of validation, Section 5 presents a concrete-like case to illuminate the performances of the model. This numerical example helps us to clarify the role of closure for the hysteresis phenomenon. Subsequently, in Section 6, the model is further examined by comparing it with experimental results provided by Piotrowska (2013). Three different types of inclusions are used to build concretes in experiments, making it a very suitable example to illustrate the effect of the interfaces for a heterogeneous material. By applying the same formulations and loadings, the proposed model succeeds in reproducing the macroscopic responses for monotonic and cyclic tests. Finally, a brief conclusion and discussion are addressed in Section 7 to close the paper.

## Nomenclature

| | |
|---|---|
| $\boldsymbol{B}$ | standard strain interpolation matrix |
| $\boldsymbol{d}$ | nodal displacements |
| $\boldsymbol{\epsilon}$ | strain field |
| $\boldsymbol{H}_{\mathrm{w}}$ | equivalent normal vector matrix |
| $\boldsymbol{K}$ | stiffness matrix |
| $\boldsymbol{n}$ | normal vector on the discontinuity surface |
| $\boldsymbol{n}_p$ | sliding direction on the discontinuity surface, corresponding to the "position" of the sliding |
| $\boldsymbol{n}_t$ | shear vector on the discontinuity surface, corresponding to the "tendency" of the sliding |
| $\mathcal{S}_\epsilon$ | weak discontinuities such as heterogeneity interfaces |
| $\boldsymbol{\sigma}$ | stress field |
| $\mathcal{S}_u$ | strong discontinuities such as cracks and fractures |
| $\boldsymbol{T}$ | traction vector on the discontinuity surface |
| $\boldsymbol{T}_n$ | normal stress on the discontinuity surface |
| $\boldsymbol{T}_t$ | shear stress on the discontinuity surface |
| $\boldsymbol{u}$ | theoretical displacement field |
| $\boldsymbol{C}$ | elastic stiffness matrix of the Hooke's law |
| $\delta_{\mathcal{S}_u}$ | Dirac-delta distribution that centered at the discontinuity surface |
| $[\lvert\boldsymbol{\epsilon}\rvert]$ | jump in the strain field |

| | |
|---|---|
| $[\|\boldsymbol{u}\|]$ | jump in the displacement field |
| $\Gamma$ | closed boundary of the reference body |
| $\Gamma_t$ | traction boundary of the reference body |
| $\Gamma_u$ | displacement boundary of the reference body |
| $\mathcal{G}_{\text{op}}$ | fracture energy, which represents the necessary energy to create a fully opened crack |
| $\mathbf{G}_{\text{s}}$ | strong enhanced strain interpolation matrix of the actual field |
| $\mathbf{G}_{\text{s}}^{*}$ | strong enhanced interpolation matrix of the virtual field |
| $\mathbf{G}_{\text{w}}$ | weak enhanced strain interpolation matrix of the actual field |
| $\hat{\boldsymbol{u}}$ | arbitrary displacement field |
| $\mathcal{H}_{\mathcal{S}_u}$ | Heaviside function that centered at the discontinuity surface |
| $\Omega$ | reference domain in 3D |
| $\Omega_e$ | discretized finite element |
| $\overline{\boldsymbol{u}}$ | regular displacement field |
| $\tilde{\bullet}/\hat{\bullet}$ | weak/strong discontinuity |
| $\varphi$ | friction angle of the Mohr-Coulomb criterion |
| $\varphi_e$ | continuous arbitrary function which has null value at $\Omega^-$ and unit value at $\Omega^+$ |
| $C$ | cohesion of the Mohr-Coulomb criterion |
| $E$ | Young's module |
| $N$ | shape function of the finite element |
| $V$ | volume |
| $\bullet^+/\bullet^-$ | upper/lower part of the sub-domain $\Omega^+$ and $\Omega^+$ |

## 2. Weak form of the weak and strong enhancements kinematics

We present in this section the kinematics descriptions of the weak and strong discontinuities. We start by summarizing the basic notations that are employed in this paper. A graphic of the reference domain $\Omega$ is drawn in Fig. 1. The dark gray part states for the heterogeneity, and the light gray part represents the matrix. The solid can be discretized within the Finite Element Method by using an unstructured mesh, which results in a set of elements $\Omega_e$.

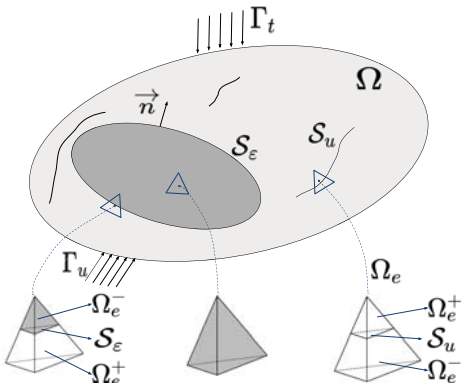


**Figure 1:** Illustration of the considered solid which exhibits weak and strong discontinuities.

The weak discontinuity exists in the elements which are situated between two phases and are passed through by the interface $\mathcal{S}_\epsilon$ between them. A jump in the strain field $[|\boldsymbol{\varepsilon}|]$ is embedded in these elements because of the difference between the material parameters, see Fig. 2(a). The strong discontinuity represents the cracks and fractures such as $\mathcal{S}_u$ in Fig. 1. The element of this type carries a jump in the displacement field $[|\boldsymbol{u}|]$. Here, only mode-II discontinuity is considered, see Fig. 2(b). In the case of exhibiting both discontinuities on the heterogeneity interface, a debonding at the heterogeneity can be represented, see Fig. 2(c). An orthogonal basis $(\boldsymbol{n}, \boldsymbol{m}, \boldsymbol{t})$ is built based on the normal vector $\boldsymbol{n}$ of the discontinuity surface.

It is considered that the weak and strong discontinuities are independent and additive, the total strain field is written

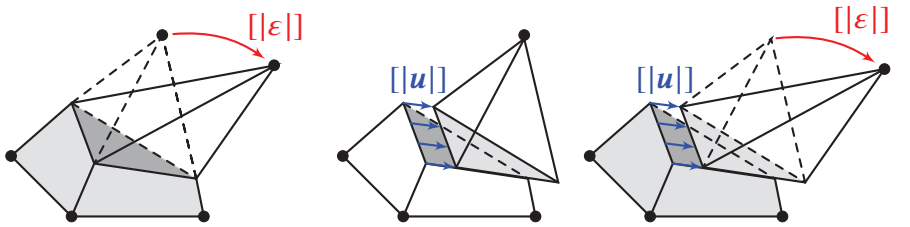


(a) Weak discontinuity (b) Strong discontinuity (c) Both weak and strong discontinuity

**Figure 2:** Three cases of discontinuities on a tetrahedral element (modified from Roubin, Stamati, Ando and Malecot (2019)).

as (Simo and Rifai, 1990):

$$\boldsymbol{\varepsilon} = \underbrace{\nabla^{\mathrm{sym}}\overline{\boldsymbol{u}}}_{\text{regular}} + \underbrace{\tilde{\boldsymbol{\varepsilon}}}_{\text{weak}} + \underbrace{\hat{\boldsymbol{\varepsilon}}}_{\text{strong}}, \tag{1}$$

where $\overline{\boldsymbol{u}}$ is the regular displacement, $\nabla^{\mathrm{sym}}$ is the symmetric gradient operator, and $\tilde{\bullet}(\hat{\bullet})$ refers to the weak (strong) enhancement (Benkemoun et al.). Their kinematic descriptions are introduced in the following parts.

## 2.1. Kinematical description of the weak discontinuity

As presented in the previous part, the weak discontinuity exhibits in an element which is located between two phases and carries two types of materials. The weak enhanced strain field is denoted as $\tilde{\boldsymbol{\varepsilon}}$. Correspondingly, the weak enhanced part of the displacement field is noted as $\tilde{\boldsymbol{u}}$ with $\tilde{\boldsymbol{\varepsilon}} := \nabla^{\mathrm{sym}}\tilde{\boldsymbol{u}}$, and defined as $\tilde{\boldsymbol{u}}^+$ in the sub-volume $\Omega_e^+$, $\tilde{\boldsymbol{u}}^-$ in the sub-volume $\Omega_e^-$. The jump in the strain field is therefore defined as $[|\boldsymbol{\varepsilon}|] := \boldsymbol{\varepsilon}^+ - \boldsymbol{\varepsilon}^-$.

Regarding the weak discontinuity diagram in Fig. 2(a), two conditions can be deduced. A first condition is proposed to respect the continuity of the displacement field at the discontinuity interface. A second condition takes its origin from the physical consideration of the smoothness of the displacement field: the displacement derivatives are only discontinuous in the direction perpendicular to the discontinuity surface (following direction $\boldsymbol{n}$). Therefore, the jump in the strain field can be entirely defined by three unknown values: $\{[\varepsilon]_n, [\varepsilon]_m, [\varepsilon]_t\}^{\mathrm{T}}$ (Roubin et al., 2015).

For a finite element which carries one weak discontinuity, the displacement field can be expressed in a first-order form (Ibrahimbegovic, Markovic, Matthies, Niekamp and Taylor, 2005):

$$\tilde{\boldsymbol{u}}(\boldsymbol{x}) = \Theta\boldsymbol{n}\cdot(\boldsymbol{x}-\boldsymbol{\xi})([\varepsilon]_n\boldsymbol{n} + [\varepsilon]_m\boldsymbol{m} + [\varepsilon]_t\boldsymbol{t}) \text{ with } \Theta = \begin{cases} \Theta^+ & \forall x \in \Omega_e^+ \\ \Theta^- & \forall x \in \Omega_e^- \end{cases}, \tag{2}$$

where $\Theta$ is a still undefined function (the specific definition is introduced later), $\xi$ stands for the position of the discontinuity surface, and thus $\boldsymbol{n}\cdot(\boldsymbol{x}-\boldsymbol{\xi})$ acts as a signed distance to the discontinuity. Correspondingly, by taking the symmetric gradient operation, the weak enhanced part of the strain field is given as:

$$\tilde{\boldsymbol{\varepsilon}} = \nabla^{\mathrm{sym}}(\tilde{\boldsymbol{u}}) = \Theta\left([\varepsilon]_n\boldsymbol{n}\otimes\boldsymbol{n} + \frac{[\varepsilon]_m}{2}(\boldsymbol{n}\otimes\boldsymbol{m})^{\mathrm{sym}} + \frac{[\varepsilon]_t}{2}(\boldsymbol{n}\otimes\boldsymbol{t})^{\mathrm{sym}}\right). \tag{3}$$

## 2.2. Kinematics description of the strong discontinuity

We consider in this part an element that carries a displacement discontinuity. Here, from a meso-scale point of view, the discontinuity is considered as micro-cracks (Simo et al., 1993; Oliver, 1996a,b; Wells, 2001). The kinematics description of the displacement field can be mathematically decomposed:

$$\boldsymbol{u} = \overline{\boldsymbol{u}} + \mathcal{H}_{S_u}[|\boldsymbol{u}|] = \hat{\boldsymbol{u}} + (\mathcal{H}_{S_u} - \varphi_e)[|\boldsymbol{u}|], \tag{4}$$

with $\boldsymbol{u}$ is the theoretical displacement field, $\overline{\boldsymbol{u}}$ is the regular displacement, $\hat{\boldsymbol{u}}$ is the arbitrary displacement that we can apply the boundary conditions, they have a relationship of $\hat{\boldsymbol{u}} = \overline{\boldsymbol{u}} + \varphi_e[|\boldsymbol{u}|]$, and $(\mathcal{H}_{S_u} - \varphi_e)[|\boldsymbol{u}|]$ stands for the

discontinuous part. In this function, $\mathcal{H}_{\mathcal{S}_u}$ is the Heaviside function which is centered at the discontinuity surface, $\varphi_e$ is an arbitrary function with null value at $\Omega^-$ and unit value at $\Omega^+$, and $[|\boldsymbol{u}|]$ is a continuous function on $\Omega_e$ which represents the displacement jump. An one-dimensional example is shown here to illustrate the decomposition of the displacement field, see Fig. 3.

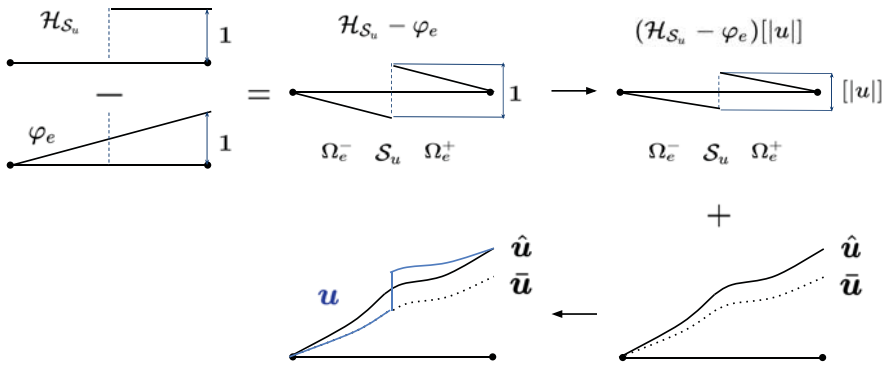


**Figure 3:** An one-dimension decomposition of the displacement field.

By taking a standard symmetric gradient operation to the displacement field, the strain field is obtained as (Simo and Oliver, 1994):

$$\boldsymbol{\varepsilon} = \nabla^{\text{sym}}\boldsymbol{u} = \underbrace{\nabla^{\text{sym}}\hat{\boldsymbol{u}}}_{\text{regular}} + \underbrace{(\mathcal{H}_{\mathcal{S}_u} - \varphi_e)\nabla^{\text{sym}}([|\boldsymbol{u}|]) - ([|\boldsymbol{u}|] \otimes \nabla\varphi_e)^{\text{sym}}}_{\text{bounded enhancement } \hat{\varepsilon}_b} + \underbrace{\delta_{\mathcal{S}_u}([|\boldsymbol{u}|] \otimes n)}_{\text{unbounded enhancement } \hat{\varepsilon}_u}, \tag{5}$$

where $\delta_{\Gamma_d}$ is the Dirac-delta distribution, resulting in an infinite value at the discontinuity surface on the strain field, *i.e.*, unbounded.

Since $[|\boldsymbol{u}|]$ is chosen as a constant function on $\Omega_e$, it leads to a null value of its symmetric gradient, namely *Kinematically Enhanced Strain* (KES)(Oliver, 2000). The bounded enhancement part thus refers to as:

$$\hat{\varepsilon}_b = -([|\boldsymbol{u}|] \otimes \nabla\varphi_e)^{\text{sym}}. \tag{6}$$

With the kinematic description of the weak and strong enhancements (Eq. (3) and Eq. (5)) at hands, it is recalled that these two discontinuities are independent and additive (Eq. (1)). In the case of exhibiting both discontinuities in an element, the constitutive model is employed in the same way (Benkemoun et al.).

## 3. Discrete constitutive model at the discontinuity

In this section, the focus is made on the discontinuity model at the fine mesoscale. The *strong discontinuity analysis* is first proposed by Simo et al. (1993). It aims at ensuring the consistency of the constitutive model in the presence of a strong discontinuity. The *Discrete Strong Discontinuity Approach* (DSDA) (Oliver, 2000) is used in this study:

- Beyond the strong discontinuity: the bulk volumes are assumed to be linear and continuous;
- On the discontinuity: the traction vector $\boldsymbol{T}$ is continuous through the discontinuity, serving as a bridge that links the two sub-volumes.

The mechanical description of the failure mechanism is strongly linked with the traction vector $\boldsymbol{T}$. The governing law usually associates the traction vector with the crack-opening $[|\boldsymbol{u}|]$, namely the *traction separation law* (Wells, 2001; Dias-da Costa, Alfaiate, Sluys and Júlio, 2009a,b).

In the framework of DSDA implementation, two broad families have attracted a significant amount of attention over the last two decades, namely: The Extended Finite Element Method (X-FEM) (Moës, Dolbow and Belytschko, 1999; Dolbow, Moës and Belytschko, 2000; Wells and Sluys, 2001; Belytschko, Moës, Usui and Parimi, 2001; Mariani

and Perego, 2003) and the Enhanced Finite Element Method (E-FEM). Their most striking difference is the support of the enriching mode: for the nodal enrichment models (such as X-FEM), the enhancement is attached to the nodes; for elemental enrichment models (such as E-FEM), the additional degrees of freedom are embedded inside the element (Oliver, Huespe and Sánchez, 2006). This feature brings an advantage to E-FEM models, that is, the local equilibrium equations can be solved with fixed global unknowns. Then, the static condensation procedure leads to a global system of equations, the size of which remains constant regardless of how many cracks are localised in the solid. To some extent, the E-FEM strategy can be considered as a non-intrusive one. On the other hand, the X-FEM allows the introduction of high-order interpolation functions, thus improving consistency and leading to more enhancements.

In the existing literature for the E-FEM models, mode-I traction-opening discontinuity is the common choice (Roubin et al., 2015). Mode-II sliding-opening discontinuities in 3D have been introduced in (Hauseux et al., 2016). However, to the author's knowledge, no 3D coupling of the two modes exist. Indeed, this is a major challenge that shall be considered in upcoming projects. Here, considering applications to compression loading paths, the mode-II propagation is chosen.

### 3.1. Localization criterion - Mohr-Coulomb

There are two main purposes of the localization criterion: determine the appearance of the localization, and determine the orientation of the discontinuity interface and the sliding direction. The localization criterion in this study is based on the Mohr-Coulomb criterion (Salençon, 2002). It is a widely used criterion that contains two critical parameters: the cohesion $C$ and the friction angle $\varphi$. Since the target solid contains heterogeneities (weak discontinuities), two cases have to be considered.

In the case of homogeneous element, the element carries no geometrical information on the orientation of the discontinuity interface. The localization criterion gives as (Salençon, 2002; Lemaitre, Chaboche, Benallal and Desmorat, 2009)

$$\Phi_1 = \operatorname*{Sup}_n \left( \|\boldsymbol{T}_t\| + T_n \tan\varphi - C \right), \tag{7}$$

where $\boldsymbol{T}_n/\boldsymbol{T}_t$ is the projection of the traction vector on the normal/tangent direction of the discontinuity interface:

$$\begin{cases} T_n = \boldsymbol{n} \cdot \boldsymbol{\sigma} \cdot \boldsymbol{n} \\ \|\boldsymbol{T}_t\| = \|\boldsymbol{T} - T_n \cdot \boldsymbol{n}\| = \|\boldsymbol{T} \cdot \boldsymbol{n}_t\|. \end{cases} \tag{8}$$

Here, the normal vector of the discontinuity interface is defined on the surface which maximizes the criterion Eq. (7), and the sliding direction follows the traction vector on the discontinuity surface $\boldsymbol{T}_t$.

In the case of an element with a weak discontinuity, it is assumed that the strong discontinuity appears along the same interface. Thus, the normal unit vector of this interface is predefined and the sliding orientation is determined by the maximum shear stress. This assumption is consistent with the experimental fact: dealing with concrete, cracks appear at the interface between mortar and aggregates. This is mainly due to the Interfacial Transition Zone (ITZ) (Scrivener, Crumbie and Laugesen, 2004; Jebli, Jamin, Malachanne, Garcia-Diaz and El Youssoufi, 2018), which carries a higher porosity.

Representing the Mohr-Coulomb criterion in a diagram, see Fig. 4, the area under the curves corresponds to an elastic mechanism (marked in gray), while on the curve corresponds to the localization criterion Eq. (7) equals to zero and the localization occurs in the element. Once the localization apparent in the element, the orientation of the discontinuity surface is fixed throughout the computation. No rotation of the crack is considered in this study.

### 3.2. Traction separation law - Sliding opening

The sliding opening procedure occurs after the localization. It describes the failure behaviors of the material. Physically, the degradation of the element at the sliding opening phase is strongly linked with the friction between the lips of cracks. As it is drawn in Fig. 5, the force originates in the friction zone. As the sliding procedure goes on, the two sub-domains loss progressively their contact, the roughness at the friction zone decreases, and part of the rough extremities are crushed by the stress concentration. These ingredients lead to a result that the friction between the crack weakens as the sliding goes on, and this procedure is irreversible. A classical softening law is used here to describe this procedure (Vallade, 2016; Hauseux et al., 2016):

$$\Phi_o = \sigma_{\text{eq}} - \underbrace{C \exp(-C[u]/\mathcal{G}_{\text{op}})}_{C'}, \text{ with } \sigma_{\text{eq}} = \|\boldsymbol{T}_t\| + T_n \tan\varphi. \tag{9}$$

**Figure 4:** Illustration of the localization criterion in the Mohr-Coulomb diagram.

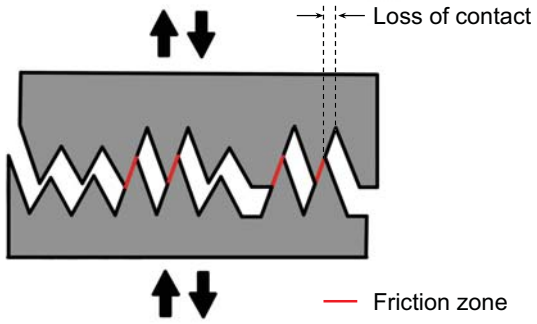


**Figure 5:** Concept of the frictional sliding between the lips of crack (Mihai and Jefferson, 2011).

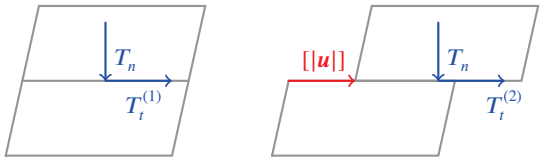


(a) Localization (b) Sliding opening

**Figure 6:** Sliding opening procedure of a 2D element, from (a) the localization to (b) the sliding opening.

In this equation, the fracture energy $\mathcal{G}_{\text{op}}$ is a local parameter of the material, representing the necessary dissipate energy for complete sliding-opening (gray area in Fig. 7(b)). The absolute value of sliding is noted as $[u]$. The relationship between the absolute value of sliding-opening and the oriented sliding vector writes as:

$$[|\boldsymbol{u}|] = [u] \cdot \boldsymbol{n}_p. \tag{10}$$

Located at the discontinuity interface, we note:

- $\boldsymbol{n}_p$: the sliding direction (Eq. (10)), corresponding to the vector which points to the "position" of the crack;
- $\boldsymbol{n}_t$: the direction of shear stress (Eq. (8)), corresponding to the sliding "tendency" of the sliding.

In the sliding opening procedure, these two vectors are equivalent.

For the sake of clarification, it is proposed here a 2D example of a single cubic element, see Fig. 6. In the following parts, the same 2D example is going to be used to represent the local constitutive behaviors at different stages. It is

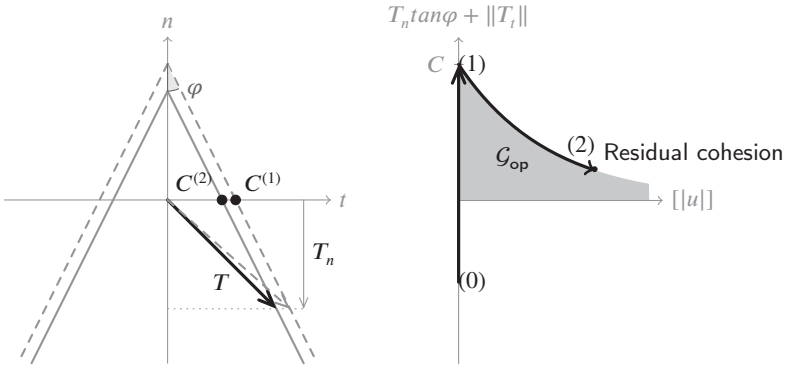


(a) Sliding opening criterion in a Mohr-Coulomb diagram

(b) Kinematic relationship between the equivalent stress and sliding opening value

**Figure 7:** Sliding opening mechanism of the local constitutive model at the discontinuity interface.

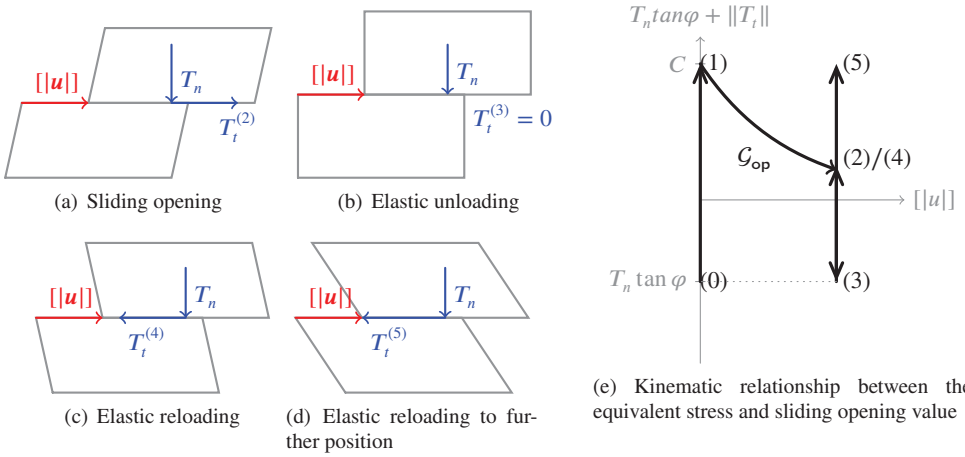


(a) Sliding opening

(b) Elastic unloading

(c) Elastic reloading

(d) Elastic reloading to further position

(e) Kinematic relationship between the equivalent stress and sliding opening value

**Figure 8:** Local constitutive behavior of the model without closure in the case of sliding backward.

assumed that the normal stress $T_n$ remains constant and compressive, and the notation $T_t^{(i)}$ and $C^{(i)}$ represent the corresponding shear stress and the cohesion at the status number $(i)$, see for example Fig. 7. As the crack opening increases, it is considered that the friction between the two sub-domains decreases. Shown in Fig. 7(a), it corresponds to a contraction of the elastic region; and shown in Fig. 7(b), it corresponds to the decreasing value of the equivalent stress.

### 3.3. Traction separation law - Sliding closing

For the model without closure, the sliding-opening value $[|\boldsymbol{u}|]$ will stay the same in the case of sliding backward, see Fig. 8. From the unloading phase (Fig. 8(b)) to the reloading phase (Fig. 8(c) and Fig. 8(d)), the model presents a pure elastic behavior. As a result, there will be no occurrence of energy dissipation. Readers can also refer to Section. 4.4 for more details.

Based on existing works on the strong discontinuity of mode-II, a closure mechanism is proposed in this section. Due to practical constraints, a simplification on the sliding direction is applied to the model. It is considered that once the sliding direction is determined at the localization, the subsequent closing orientation can only remain the same or become opposite to it. Also, the value of sliding distance $[u]$ is never negative, the sliding between sub-domains is represented by $[|\boldsymbol{u}|]$ which equals to $[u]\boldsymbol{n}_p$.

As the loading discharges and switches to the opposite direction, a series of mechanical phases occur to the discrete discontinuity, see Fig. 9. These different phases are detailed in the following parts.

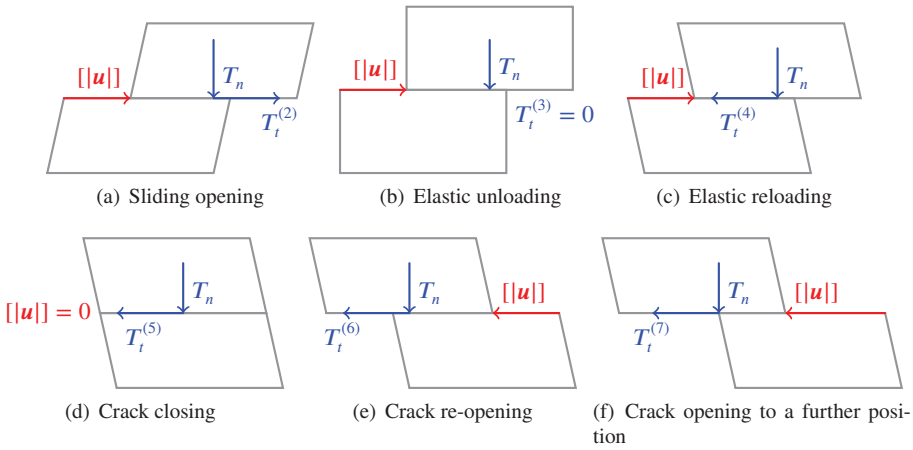


(a) Sliding opening (b) Elastic unloading (c) Elastic reloading

(d) Crack closing (e) Crack re-opening (f) Crack opening to a further position

**Figure 9:** Decomposed phases of the closing mechanism in a 2D example.

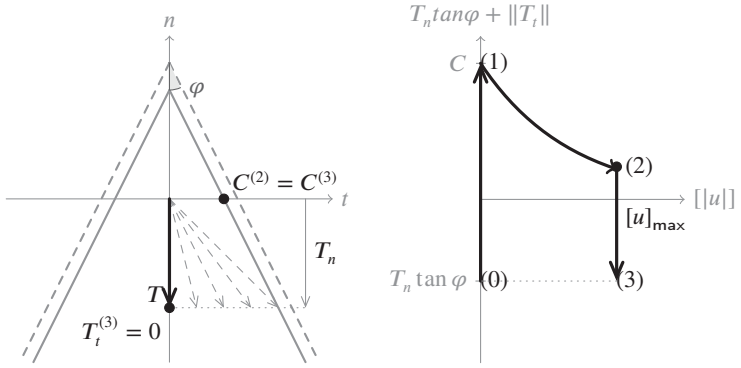


(a) Unloading procedure in a Mohr-Coulomb diagram (b) Kinematic relationship between the equivalent stress and sliding opening value

**Figure 10:** Local constitutive model at the discontinuity interface during the elastic unloading procedure.

**Elastic unloading procedure** Supposing that the loading begins to decrease, an unloading process will occur after the sliding opening phase. The elastic energy that has been stored in the element will first be released.

From Fig. 9(a) to Fig. 9(b), an unloading procedure is applied to the 2D example. Supposing that the normal stress on the discontinuity surface $T_n$ is constant and compressive, the shear stress $T_t$ at the discontinuity interface will decrease to zero at the state of completely unloading. As a result, the equivalent stress $\sigma_{\text{eq}}$ equals to $T_n \tan\varphi$ at the state of $T_t = 0$, which is negative, see Fig. 10(b). As we can see from Fig. 10(a), the whole unloading process takes place only in the elastic area. The sliding opening value $[u]$ remains unchanged.

**Elastic reloading procedure** As said previously, the unloading procedure involves a pure elastic mechanism that corresponds to a release of energy that has been stored in the bulk volume. Similarly, the reloading procedure also has a pure elastic behavior which is related to a restoration of elastic energy at the bulk volume, see Fig. 11(a). At the discontinuity, the sliding opening value $[u]$ remains unchanged, while the shear stress $T_t$ at the interface increases until it reaches the critical point where the equivalent stress is equal to the residual cohesion.

At this stage, the sliding direction $\boldsymbol{n}_p$ remains unchanged since the sliding opening $[|\boldsymbol{u}|]$ is always the same. The direction of the shear stress $\boldsymbol{n}_t$ becomes opposite to itself, see Fig. 9(c).

**Sliding back - crack closing and re-opening procedure** The sliding back procedure consists of two steps, the so-called "closure" of the micro-crack (Fig. 9(d)) and the "re-opening" phase (Fig. 9(e)). Here, it corresponds to a

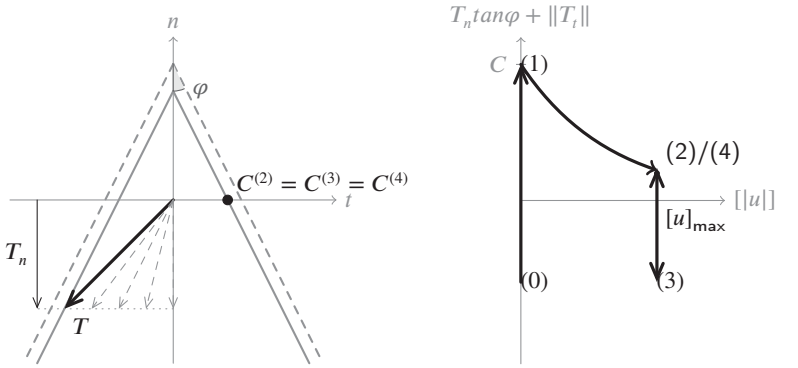


(a) Reloading procedure in a Mohr-Coulomb diagram

(b) Kinematic relationship between the equivalent stress and sliding opening value

**Figure 11:** Local constitutive model at the discontinuity interface during the elastic reloading procedure.

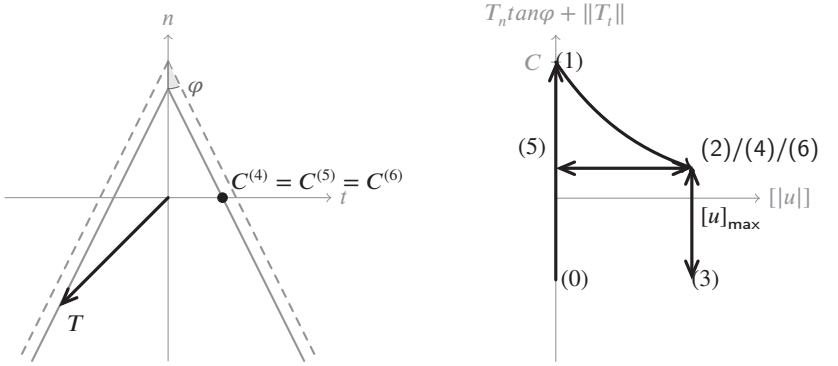


(a) Closing and reopening procedure in a Mohr-Coulomb diagram

(b) Kinematic relationship between the equivalent stress and sliding opening value

**Figure 12:** Local constitutive model at the discontinuity interface during the sliding closing and re-opening phases.

frictional sliding in the opposite direction to its original sliding orientation.

As stated previously, the friction between the lips of cracks irreversibly decreases during the sliding opening proceeds. In this study, it is assumed that the residual cohesion $C'$ remains constant during the crack closing and re-opening phases because the crack slides along the ancient trajectory.

Plotted in the local constitutive model as in Fig. 12(b), the crack closing procedure matches point (4) to point (5), and the re-opening procedure matched point (5) to point (6). It can be seen that the residual cohesion $C'$ and the traction vector $\boldsymbol{T}$ stay unchanged in this phase.

Once the sliding opening value reaches the previous maximum opening value $[u]_{\max}$, the equivalent stress is equal to the corresponding residual cohesion, the sliding opening procedure is then activated with the same governing law Eq. (9). The frictional crack starts to open to a further position, and the residual cohesion continues to decrease. Physically, this means that the "roughness" at the discontinuity interface continues to decrease as the fracture develops towards a further position. It corresponds to the procedure from Fig. 9(e) to Fig. 9(f), or point (6) to point (7) in Fig. 13.

In summary, the mechanism behaviors at the discontinuity interface are built upon the following assumptions:

- Once the sliding direction is fixed during the opening phase, the crack evolution always follows the same/opposite direction.

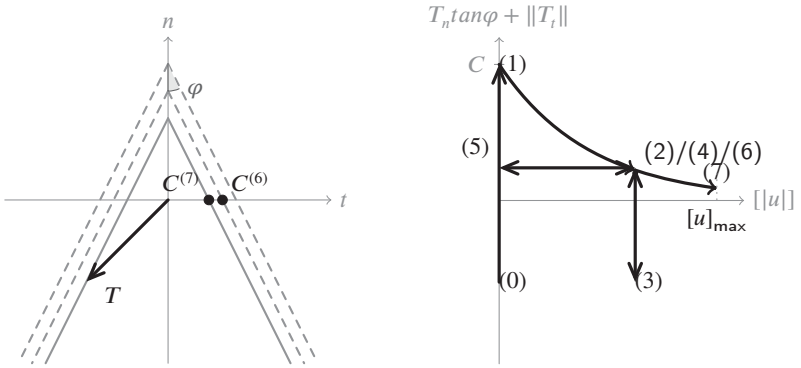


(a) Opening procedure in a Mohr-Coulomb diagram

(b) Kinematic relationship between the equivalent stress and sliding opening value

**Figure 13:** Local constitutive model at the discontinuity interface during the opening procedure after the closure.

- Residual cohesion is related to the friction at the discontinuity surface. It is considered, in order to model the erosion of the friction zone, that the friction decreases during the sliding opening phase.
- The residual cohesion is considered to decrease only if the crack extends to a new further position which exceeds $[u]_{\max}$. In other words, if the crack closes along the previous path, the residual cohesion is considered to remain constant. This assumption makes the numerical implementation simpler. Yet, it is probably not the best choice for cycling loading at a constant amplitude. Indeed, in this case, the potential wear could not be represented.

Upon considerations, the closing criterion writes as:

$$\Phi_{\mathrm{c}} = T_n \tan\varphi + \|\boldsymbol{T_t}\| - C \exp(-\frac{C[u]_{\max}}{\mathcal{G}_{\mathrm{op}}}). \tag{11}$$

The closing criterion requires no additional parameters. It is a linear equation, thus benefit from its simplification and an analytical solution is available for the resolution, readers can refer to section 4.3 for more details.

## 4. Finite Element approximation and resolution

This section deals with the resolution of the E-FEM model in a standard Finite Element framework. The difficulty is focused on the treatment of the enhancements at the discontinuity and the resolution of the additional unknown variables $[|\boldsymbol{u}|]$ and $[|\boldsymbol{\varepsilon}|]$. The implementation is based on a three-field variational formulation (Washizu, 1968). The three fields stands for the displacement, strain, and stress field. The main idea is to propose two sets of independent fields, which refer to as the standard fields $(\boldsymbol{u}, \boldsymbol{\varepsilon}, \boldsymbol{\sigma})$, and the virtual fields $(\boldsymbol{\eta}, \boldsymbol{\gamma}, \boldsymbol{\tau})$. By using the *Statically and Kinematically Optimal Nonsymmetric Formulation* (SKON) (Dvorkin, Cuitiño and Gioia, 1990; Oliver, 1996a), the actual and virtual strain fields are not interpolated the same way. The system is inevitable non symmetrical but the zero mean condition and the kinematic representation of the discontinuity can both be respected. Then the three-field variational statements is further developed by operating the Enhanced Assumed Strain method (Simo and Rifai, 1990), where the strain field is decomposed into compatible part and incompatible part. We eliminate the stress field from the formulation by an orthogonal condition between the space of the stress field and the enhanced strain field. The displacement jump is included in the variational formulation via the appearance of the Dirac-delta distribution in the enhanced strain field (Wells and Sluys, 2000). With the mixed formulations at hand, we present subsequently the resolution of the Finite Element system. Finally, a single tetrahedral element example is introduced to illustrate the validation of the resolution.

### 4.1. Finite Element discretization with double enhancements

Based on pioneer studies, the discretized solving system of a E-FEM model with both strong and weak discontinuities is given as (Benkemoun et al.; Roubin et al., 2015):

$$\bar{\mathcal{R}} := \mathop{\mathbb{A}}_{e=1}^{n_\mathrm{e}} \left(\bar{\boldsymbol{f}}_{\mathrm{int}} - \bar{\boldsymbol{f}}_{\mathrm{ext}}\right) = \mathop{\mathbb{A}}_{e=1}^{n_\mathrm{e}} \left( \bar{\boldsymbol{f}}^e_{\mathrm{ext}} - \int_{\Omega_e} \boldsymbol{B}^T \check{\boldsymbol{\sigma}}(\boldsymbol{d}, [|\boldsymbol{\varepsilon}|], [|\boldsymbol{u}|]) d\Omega \right) = \bar{0}, \tag{12a}$$

$$\bar{\mathcal{R}}^e_{[|\boldsymbol{\varepsilon}|]} = \int_{\Omega_e} \mathbf{G}_\mathrm{w}^T \check{\boldsymbol{\sigma}}(\boldsymbol{d}, [|\boldsymbol{\varepsilon}|], [|\boldsymbol{u}|])\, d\Omega = \bar{0}\,, \tag{12b}$$

$$\bar{\mathcal{R}}^e_{[|\boldsymbol{u}|]} = \int_{\Omega_e} \boldsymbol{G}_\mathrm{s}^{*,T} \check{\boldsymbol{\sigma}}(\boldsymbol{d}, [|\boldsymbol{\varepsilon}|], [|\boldsymbol{u}|])\, d\Omega = \int_{\Omega_e \setminus S} \mathbf{G}_{\mathrm{s,b}}^{*,T} \check{\boldsymbol{\sigma}}(\boldsymbol{d}, [|\boldsymbol{\varepsilon}|], [|\boldsymbol{u}|]) d\Omega + \int_S \boldsymbol{T} d\partial\Omega = \bar{0}, \tag{12c}$$

where the behavior law respects the Hooke's law:

$$\check{\boldsymbol{\sigma}}(\boldsymbol{d}, [|\boldsymbol{\varepsilon}|], [|\boldsymbol{u}|]) = \begin{cases} \boldsymbol{C}^+ \boldsymbol{\varepsilon}^+ = \boldsymbol{C}^+ (\boldsymbol{B}\boldsymbol{d} + \mathbf{G}_\mathrm{w}^+ [|\boldsymbol{\varepsilon}|] + \boldsymbol{G}_s [|\boldsymbol{u}|]), \forall \boldsymbol{x} \in \Omega^+, \\ \boldsymbol{C}^- \boldsymbol{\varepsilon}^- = \boldsymbol{C}^- (\boldsymbol{B}\boldsymbol{d} + \mathbf{G}_\mathrm{w}^- [|\boldsymbol{\varepsilon}|] + \boldsymbol{G}_s [|\boldsymbol{u}|]), \forall \boldsymbol{x} \in \Omega^-. \end{cases} \tag{13}$$

In this equation, the matrix $\boldsymbol{C}^{+|-}$ is the stiffness matrix for the sub-domains $\Omega_e^{+|-}$, $\boldsymbol{B}$ is the standard strain interpolation matrix, and $(\boldsymbol{d}, [|\boldsymbol{\varepsilon}|], [|\boldsymbol{u}|])$ is the three unknown variables to be solved, corresponding to the displacement field, jump in the strain field, and jump in the displacement field.

The discretized equation Eq. (12a) depicts the global system, with $\mathop{\mathbb{A}}_{e=1}^{n_\mathrm{e}}$ is the standard assembly operation, and $\bar{\boldsymbol{f}}^e_{\mathrm{ext}}/\bar{\boldsymbol{f}}^e_{\mathrm{int}}$ stands for the external/internal force vectors. The equations Eq. (12b) and Eq. (12b) correspond separately to the weak and strong discontinuity, which is solved at the element level. Several interpolation matrix of the enhanced strain field, $\mathbf{G}_\mathrm{w}, \mathbf{G}_\mathrm{s}, \mathbf{G}_\mathrm{s}^*$, are introduced in Eq. (12) and Eq. (13). Since it has been well documented in existing studies (Roubin et al., 2015), the developments are not detailed here. The explicit expressions are given in Appendix A.

### 4.2. Linearization of the strong discontinuity

The discretized equation for the strong discontinuity is given in Eq. (12c). It can be seen that the traction vector is formulated in the system. Assuming that the discontinuity surface is a plane, the traction vector $\boldsymbol{T}$ can be calculated by taking the average value of $\check{\boldsymbol{\sigma}}$:

$$\boldsymbol{T} = \frac{1}{V} \boldsymbol{H}_\mathrm{s}^{*,T} (V^+ \check{\boldsymbol{\sigma}}^+ + V^- \check{\boldsymbol{\sigma}}^-), \tag{14}$$

where $V^{+|-}$ is the volume for the sub-domain $\Omega_e^{+|-}$. Following Ibrahimbegović, Gharzeddine and Chorfi (1998), the traction separation law is incorporated in the system through the traction vector.

If the element is in the sliding opening phase, the governing law is described by Eq. (9). Written in an incremental form, $\Phi_\mathrm{o}$ gives as:

$$\Delta\Phi_\mathrm{o} = \frac{\partial \sigma_{\mathrm{eq}}}{\partial \boldsymbol{T}} \Delta \boldsymbol{T} + \frac{\partial \boldsymbol{C}'}{\partial [u]} \Delta [u]. \tag{15}$$

Given that the equivalent stress is calculated as $\sigma_{\mathrm{eq}} = \|\boldsymbol{T_t}\| + T_n \tan\varphi$, we have $\partial\sigma_{\mathrm{eq}}/\partial \boldsymbol{T} = \boldsymbol{n}_t + \boldsymbol{n}\tan\varphi$. The linearized equation of the strong discontinuity in the sliding opening phase writes as:

$$\Delta\Phi_\mathrm{o} = \underbrace{(\boldsymbol{n}_t + \boldsymbol{n}\tan\varphi)\frac{1}{V}\boldsymbol{H}_\mathrm{s}^{*,T}(V^+\boldsymbol{C}^+ + V^-\boldsymbol{C}^-)\boldsymbol{B}}_{\boldsymbol{K}_{\mathrm{s}^*\mathrm{b}}} \Delta\boldsymbol{d} + \underbrace{(\boldsymbol{n}_t + \boldsymbol{n}\tan\varphi)\frac{V^+V^-}{V}\boldsymbol{H}_\mathrm{s}^{*,T}(\boldsymbol{C}^+ - \boldsymbol{C}^-)\boldsymbol{H}_\mathrm{w}}_{\boldsymbol{K}_{\mathrm{s}^*\mathrm{w}}} \Delta[|\boldsymbol{\varepsilon}|]$$

$$+\underbrace{(\boldsymbol{n}_t+\boldsymbol{n}\tan\varphi)\frac{1}{V}\boldsymbol{H}_{\mathrm{s}}^{*,T}(V^{+}\boldsymbol{C}^{+}+V^{-}\boldsymbol{C}^{-})\boldsymbol{G}_s\boldsymbol{n}_p}_{\boldsymbol{K}_{\mathrm{s}^*\mathrm{s}}}\Delta[u]$$

$$+\underbrace{\frac{C^2}{\mathcal{G}_{\mathrm{op}}}e^{-C[u]/\mathcal{G}_{\mathrm{op}}}}_{K_{\mathrm{qo}}}\Delta[u]. \tag{16}$$

If the element is in the sliding closing phase, the procedure is governed by Eq. (11). In this case, the closing criterion $\Phi_{\mathrm{c}}$ contains only one variable, the linearization equation writes as:

$$\begin{aligned}\Delta\Phi_{\mathrm{c}} &= \frac{\partial\sigma_{\mathrm{eq}}}{\partial\boldsymbol{T}}\Delta\boldsymbol{T}\\ &= \boldsymbol{K}_{\mathrm{s}^*\mathrm{b}}\Delta\boldsymbol{d}+\boldsymbol{K}_{\mathrm{s}^*\mathrm{w}}\Delta[|\boldsymbol{\varepsilon}|]+\boldsymbol{K}_{\mathrm{s}^*\mathrm{s}}\Delta[|\boldsymbol{u}|].\end{aligned}$$

The terms $\boldsymbol{K}_{\mathrm{s}^*\mathrm{b}}, \boldsymbol{K}_{\mathrm{s}^*\mathrm{w}}, \boldsymbol{K}_{\mathrm{s}^*\mathrm{s}}$ in this equation are defined as the same as in Eq. 16.

### 4.3. Resolution strategy

The linearization of the solving system can be written in a matrix form in terms of the increments $(\boldsymbol{d}, [|\boldsymbol{\varepsilon}|], [|\boldsymbol{u}|])$:

- If the element is in the sliding-opening phase (Roubin et al., 2015):

$$\begin{bmatrix}\boldsymbol{K}_{\mathrm{bb}} & \boldsymbol{K}_{\mathrm{bw}} & \boldsymbol{K}_{\mathrm{bs}}\\ \boldsymbol{K}_{\mathrm{wb}} & \boldsymbol{K}_{\mathrm{ww}} & \boldsymbol{K}_{\mathrm{ws}}\\ \boldsymbol{K}_{\mathrm{s}^*\mathrm{b}} & \boldsymbol{K}_{\mathrm{s}^*\mathrm{w}} & \boldsymbol{K}_{\mathrm{s}^*\mathrm{s}}+K_{\mathrm{qo}}\end{bmatrix}_{n+1}^{(k)}\begin{Bmatrix}\Delta\boldsymbol{d}\\ \Delta[|\boldsymbol{\varepsilon}|]\\ \Delta[u]\end{Bmatrix}_{n+1}^{(k+1)}=\begin{Bmatrix}-(\boldsymbol{f}_{\mathrm{int}}^{e}-\boldsymbol{f}_{\mathrm{ext}}^{e})\\ -\mathcal{R}_{[|\boldsymbol{\varepsilon}|]}^{e}\\ -\Phi_{\mathrm{o}}\end{Bmatrix}_{n+1}^{(k)}, \tag{17}$$

- If the element is in the sliding-closing phase:

$$\begin{bmatrix}\boldsymbol{K}_{\mathrm{bb}} & \boldsymbol{K}_{\mathrm{bw}} & \boldsymbol{K}_{\mathrm{bs}}\\ \boldsymbol{K}_{\mathrm{wb}} & \boldsymbol{K}_{\mathrm{ww}} & \boldsymbol{K}_{\mathrm{ws}}\\ \boldsymbol{K}_{\mathrm{s}^*\mathrm{b}} & \boldsymbol{K}_{\mathrm{s}^*\mathrm{w}} & \boldsymbol{K}_{\mathrm{s}^*\mathrm{s}}\end{bmatrix}_{n+1}^{(k)}\begin{Bmatrix}\Delta\boldsymbol{d}\\ \Delta[|\boldsymbol{\varepsilon}|]\\ \Delta[u]\end{Bmatrix}_{n+1}^{(k+1)}=\begin{Bmatrix}-(\boldsymbol{f}_{\mathrm{int}}^{e}-\boldsymbol{f}_{\mathrm{ext}}^{e})\\ -\mathcal{R}_{[|\boldsymbol{\varepsilon}|]}^{e}\\ -\Phi_{\mathrm{c}}\end{Bmatrix}_{n+1}^{(k)}, \tag{18}$$

where the subscript $(n)$ is the label of the time step, and the superscript $(k)$ is associated with the iteration number. The explicit expressions of the assembled matrix $K$ is listed in Appendix B.

The resolution of the linearized system is done at two levels. We solve first the internal variables $(\Delta[|\boldsymbol{\varepsilon}|], \Delta[|\boldsymbol{u}|])$ at the element level for a given $\Delta\boldsymbol{d}$ by taking a null residual $\mathcal{R}_{[|\boldsymbol{\varepsilon}|]}^{e}=0$ and traction separation law $(\Phi_{\mathrm{o}}=0, \Phi_{\mathrm{c}}=0)$. Then the global equation can be solved using a static condensation (Wilson, 1974) on the solved variables $(\Delta[|\boldsymbol{\varepsilon}|], \Delta[|\boldsymbol{u}|])$. This leads to a modified stiffness matrix $\mathbb{K}_{\mathrm{sc}}$ to solved the global system:

$$\mathbb{K}_{\mathrm{sc}}\Big|_{n+1}^{(k)}\Delta\boldsymbol{d}\Big|_{n+1}^{(k+1)}=-\mathop{\mathbb{A}}_{e=1}^{n_{\mathrm{e}}}\{\boldsymbol{f}_{\mathrm{int}}^{e}-\boldsymbol{f}_{\mathrm{ext}}^{e}\}\Big|_{n+1}^{(k)}, \text{ with } \mathbb{K}_{\mathrm{sc}}\Big|_{n+1}^{(k)}=\mathop{\mathbb{A}}_{e=1}^{n_{\mathrm{e}}}\boldsymbol{K}_{\mathrm{sc}}\Big|_{n+1}^{(k)}. \tag{19}$$

The assembled matrix $\boldsymbol{K}_{\mathrm{sc}}$ is calculated separately depending on the status of the element:

- If the element is in the sliding-opening phase (Roubin et al., 2015):

$$\boldsymbol{K}_{\mathrm{sc}}\Big|_{n+1}^{(k)}=\boldsymbol{K}_{\mathrm{bb}}-\begin{bmatrix}\boldsymbol{K}_{\mathrm{bw}} & \boldsymbol{K}_{\mathrm{bs}}\end{bmatrix}\left(\begin{bmatrix}\boldsymbol{K}_{\mathrm{ww}} & \boldsymbol{K}_{\mathrm{ws}}\\ \boldsymbol{K}_{\mathrm{s}^*\mathrm{w}} & \boldsymbol{K}_{\mathrm{s}^*\mathrm{s}}+K_{\mathrm{qo}}\end{bmatrix}_{n+1}^{(k)}\right)^{-1}\begin{bmatrix}\boldsymbol{K}_{\mathrm{wb}}\\ \boldsymbol{K}_{\mathrm{s}^*\mathrm{b}}\end{bmatrix}_{n+1}^{(k)}, \tag{20}$$

- If the element is in the sliding-closing phase:

$$\boldsymbol{K}_{\mathrm{sc}}\Big|_{n+1}^{(k)}=\boldsymbol{K}_{\mathrm{bb}}-\begin{bmatrix}\boldsymbol{K}_{\mathrm{bw}} & \boldsymbol{K}_{\mathrm{bs}}\end{bmatrix}\left(\begin{bmatrix}\boldsymbol{K}_{\mathrm{ww}} & \boldsymbol{K}_{\mathrm{ws}}\\ \boldsymbol{K}_{\mathrm{s}^*\mathrm{w}} & \boldsymbol{K}_{\mathrm{s}^*\mathrm{s}}\end{bmatrix}_{n+1}^{(k)}\right)^{-1}\begin{bmatrix}\boldsymbol{K}_{\mathrm{wb}}\\ \boldsymbol{K}_{\mathrm{s}^*\mathrm{b}}\end{bmatrix}_{n+1}^{(k)}. \tag{21}$$

It can be seen that though the assembled stiffness matrix $\mathbb{K}_{sc}$ is modified by the enhancements, its size is always consistent which equals to the size of a standard stiffness matrix $\mathbb{K}_{bb}$. It leads to a convenient that the resolution can be done with constant memory, the growing number of localized elements will not increase the required computational power.

From Eq. (17) and Eq. (18), it can be seen that the non linearity of the system is only addressed on the strong discontinuity, *i.e.* the resolution of the traction separation criteria. The main purpose is to solve the unknown variable $[u]$. For the sliding opening criterion $\Phi_o$, it can be reformed into an equation in terms of $[u]$ (Roubin et al., 2015):

$$T_e + M[u] = C \exp\left(-\frac{C}{\mathcal{G}_{op}}[u]\right), \text{ with } \begin{cases} T_e &= \left(\boldsymbol{K}_{s^*b} - \boldsymbol{K}_{s^*w}\boldsymbol{K}_{ww}^{-1}\boldsymbol{K}_{wb}\right)\boldsymbol{d}, \\ M &= \left(\boldsymbol{K}_{s^*s} - \boldsymbol{K}_{s^*w}\boldsymbol{K}_{ww}^{-1}\boldsymbol{K}_{ws}\right). \end{cases} \tag{22}$$

Here, by using the Lambert W function (Corless, Gonnet, Hare, Jeffrey and Knuth, 1996), an analytical solution is available (Roubin et al., 2015):

$$[u]_{sol} = \frac{\mathcal{G}_{op}}{C}\left(W_0\left(\frac{C^2\exp(\frac{CT_e}{\mathcal{G}_{op}M})}{\mathcal{G}_{op}M}\right) - \frac{CT_e}{\mathcal{G}_{op}M}\right). \tag{23}$$

Similarly, the sliding-closing criterion $\Phi_c$ can be written in an equivalent form:

$$\Phi_c = T_e + M[u] - C\exp(-\frac{C[u]_{max}}{\mathcal{G}_{op}}). \tag{24}$$

It is a linear equation, the analytical solution for the sliding opening value $[u]$ is deduced as:

$$[u]_{sol} = \left(C\exp(-\frac{C[u]_{max}}{\mathcal{G}_{op}}) - T_e\right)/M. \tag{25}$$

Once the sliding-opening value $[u]$ is solved, the jump in the strain field is calculated as (Roubin, 2013):

$$[|\varepsilon|]_{sol} = -\boldsymbol{K}_{ww}^{-1}\left(\boldsymbol{K}_{wb}\boldsymbol{d} + \boldsymbol{K}_{ws}[u]_{sol}\right). \tag{26}$$

The model of this study is implemented in the FE code FEAP (Taylor, 1987). We use a quasi-Newton BFGS algorithm (Matthies and Strang, 1979) coupled with an iterative solver to solve the nonlinear global equation.

## 4.4. Single tetrahedral element tests

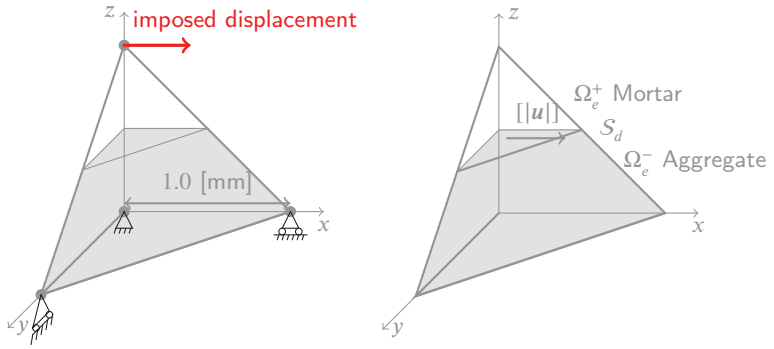


(a) Basic dimension and boundary conditions of the element

(b) Discontinuity surface apparents in the element

**Figure 14:** Basic geometric information and boundary conditions for the studied single tetrahedral element.

In order to validate the proposed model, we consider here a single tetrahedral element as an example. The element is divided into two sub-domains by an interface between two materials. The parameters are given in Table.1, and the

**Table 1**
Material parameters for the single tetrahedral element.

| Components | E [GPa] | $\nu$ [-] | $C$ [MPa] | $\tan\varphi$ | $\mathcal{G}_{\text{op}}$ $[J/m^2]$ |
|---|---|---|---|---|---|
| Mortar (white part) | 20.0 | 0.33 | 6.0 | 0.5 | 5.0 |
| Aggregate (gray part) | 70.0 | 0.33 | - | - | - |

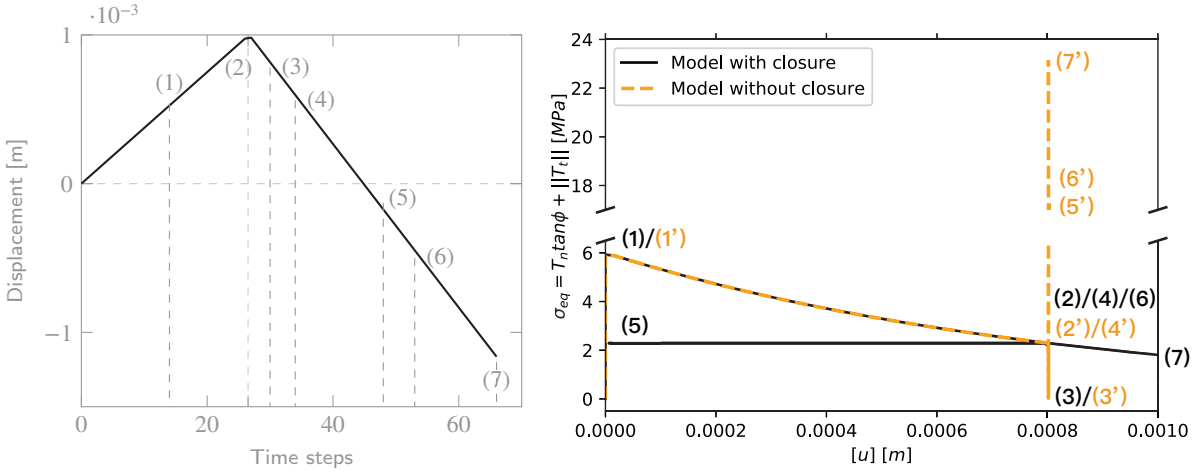


(a) Imposed displacement

(b) Comparison between the model with/without closure

**Figure 15:** Illustration of the difference between the model with and without closure by applying a non-proportional loading path (note the gap in y axis for subfigure (b)).

basic dimensions and boundary conditions of the elements are shown in Fig. 14. Here, we apply a simple occasion to the element that the normal vector of the discontinuity interface is $\boldsymbol{n} = (0, 0, 1)$, which is parallel to the $z$ axis. The imposed displacement follows the direction of the $x$ axis, which is parallel to the interface. In this case, it is easy to see that the normal vector $\boldsymbol{T}_n$ of the given interface is equal to zero. The sliding-opening $[|\boldsymbol{u}|]$ follows the same direction as the shear vector $\boldsymbol{T}_t$.

Interested in the performance of the model in a sliding forward and backward condition, the proposed displacement gives in Fig. 15(a). In order to illustrate the effect of the sliding closing mechanism, the two models are plotted in a same diagram, the main steps of the loading are also marked in the curves, see Fig. 15(b).

From Fig. 15(b), it can be seen that the model with and without closure have the same sliding opening performance. Their most obvious difference begins after the step (4). As expected, behavior of the model with closure is the same as the formulated model, see Fig. 13(b). Contrary, the model without closure cannot close the crack, the sliding-opening value $[u]$ will remain constant in the case of sliding backward (opposite to the sliding-opening direction). As consequence, the elastic response of the bulk volumes leads to a high value of shear stress $\boldsymbol{T}_t$ and equivalent stress $\sigma_{\text{eq}}$ (step (7′)).

With this validated model at hands, we now turn to the model's performances on a concrete-like material.

## 5. Illustration of the model's performances on a concrete-like material

This section is devoted to the performance of the model by applying it to a cubic concrete-like specimen. Double enhancements are embedded in the element to simulate heterogeneities and shear cracks explicitly. Particular attention is focused on the comparison between the model with and without closure. From the meso-scale to macro-scale, we attempt to reproduce several typical behaviors of concrete: i) the macroscopic failure of the material in tension and compression; ii) the typical asymmetry of tension/compression responses; iii) with the help of the closure law, the hysteresis phenomenon under cyclic loadings. In addition to the macroscopic performances of the model, crack patterns are also discussed in this section.

**Table 2**
Material parameters for the concrete-like specimen.

| Phase | E [GPa] | $\nu$ [-] | $C$ [MPa] | $\tan\varphi$ [-] | $\mathcal{G}_{\text{op}}$ $[J/m^2]$ |
|---|---|---|---|---|---|
| Matrix | 22.0 | 0.2 | 16.0 | 0.5 | 10.0 |
| Interface | - | - | 16.0 | 0.5 | 10.0 |
| Aggregate | 78.0 | 0.2 | - | - | - |

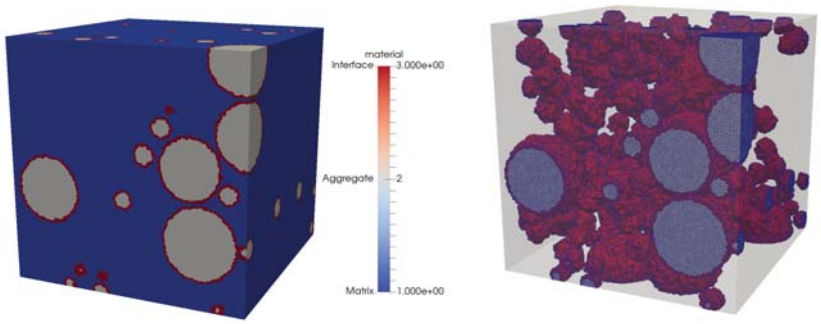


(a) Morphology of the cube with randomly positioned spheres (b) Projection to an unstructured mesh

**Figure 16:** Morphological structure of the cube and its projection to a uniformed mesh.

From a meso-scale point of view, the concrete-like solid can be seen as a bi-phase material that exhibits mortar (cement paste and small particles of sand) and hard aggregates. In this section, it is assumed that the aggregates have a pure elastic behavior. The cracks only occur in matrix elements and weakly enhanced elements. The applied parameters are gives in Table. 2. The applied loadings in this section are displacement-controlled and follow the z-axis. The lateral faces of the cube have a free stress boundary condition.

Three types of elements are illustrated in Fig. 16 by three different colors. The specimen has a length of 100 millimeters, and the volume fraction of the heterogeneities is equal to 20%. More precisely, two sets of spheres are used, which are 60% between 3 and 5 millimeters radii, and 40% between 8 and 12 millimeters radii, respectively. The hard spherical aggregates are randomly distributed in the matrix. We apply a minimum distance between each aggregate of 3 millimeters. In this case, to ensure that the weakly enhanced elements are crossed by maximum one heterogeneous interface, the size of finite elements is limited to be smaller than 2 millimeters. Herein, the mesh consists of approximately 300 000 nodes. The required calculating memory is about 1.8 GB.

## 5.1. Monotonic loadings

In this part, simple tension/compression loading is applied to the cube. The macroscopic responses of the specimen are illustrated by the macroscopic stress versus the macroscopic strain in Fig. 17.

First, the emergence of the asymmetric tension/compression response can be observed for both models with/without closure. The model with closure is slightly more ductile than another model in the post-pike phase because it dissipates more energy in closing cracks. The ratio between compressive and tensile strength is 2.7 for the model with closure, which is lower than the experimental observations. This is due to the fact that a model that exhibits pure mode-II strong discontinuities has its limitations in describing failure behavior in tension. It is a common sense that the tensile cracking pattern corresponds to an "opening" mechanism, and this model only simulates a "shear" mechanism, thus producing a higher tensile strength. In the following section, our attention is mainly focused on the behavior of materials that are associated with compressive loads.

Second, interest is made on the crack pattern for the model with closure at the softening phase. The strain is equal to $-2.0 \times 10^{-3}$, see Fig. 18. Among a large amount of localized elements that are dispersed in the material, a macro-crack can be observed in the material that passes through the cube. The angle between the macro-crack and the loading direction is around 45°. Many crack closures are observed in the material. As shown in the figure, the closure elements

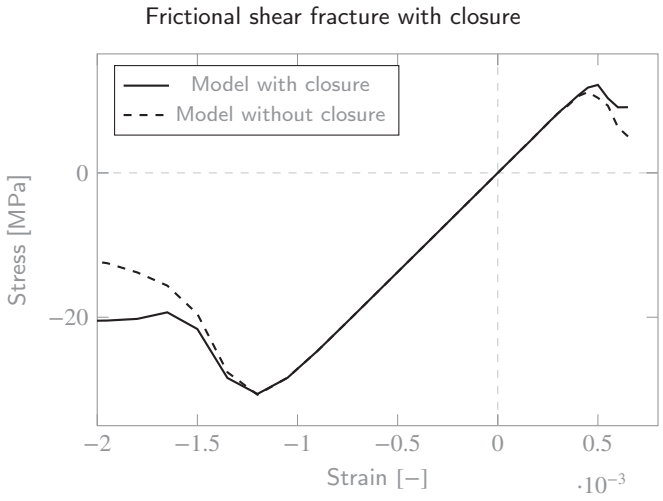


**Figure 17:** Macroscopic responses of the model with and without closure in monotonic loadings.

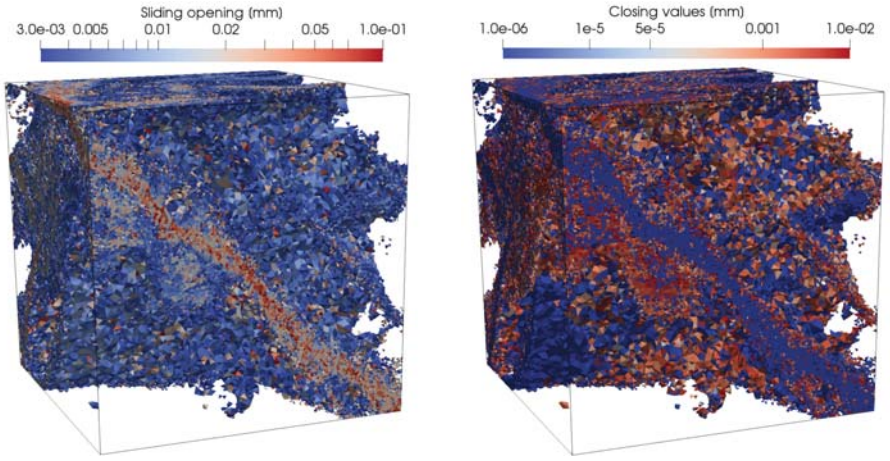


**Figure 18:** Crack pattern of the model with closures at the macroscopic strain equals to $-2.0 \times 10^{-3}$.

are located beside the main crack. They are triggered by the stress release that is caused by the rapid propagation of the failed elements in the center of the macro-crack.

Finally, we draw our attention to Fig. 19. By overlaying the macroscopic response of the material with the number of localized/closing elements, it can be noticed that the majority of the localized elements take place between the strain $[1.1 \times 10^{-3}, 1.5 \times 10^{-3}]$. This is also the period when material failure occurs. The model with and without closure have almost the same amount of localized elements. This can be explained by the fact that both models have the same localization law. The figure also shows that the closure of cracks begins after the majority of cracks have occurred. At this stage, the rate of increase in the number of localized elements is heavily reduced.

## 5.2. Cyclic loadings

Now we turn our attention to the performance of the model in cyclic loadings. The imposed displacement is plotted in Fig. 20. In order to illustrate the effect of the closure mechanism, a comparison of the macroscopic responses between the model with and without closures are plotted in Fig. 21.

It can be seen from the figure that the two models manage to produce several typical mechanical behaviors of quasi-brittle materials, such as the progressive loss of stiffness and the macroscopic plastic deformation. The material's responses in cyclic loadings are enveloped in the curves of monotonic loadings. Among several differences between these two models, the most remarkable one is that the model with closure is capable of performing hysteresis

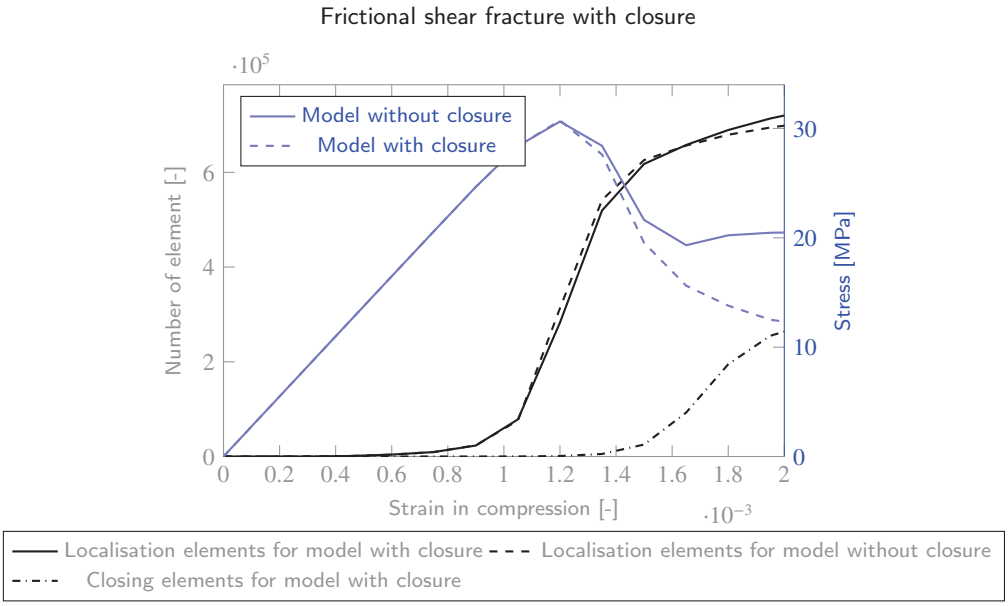


**Figure 19:** Accumulate number of elements along the compressive loading and overlaying with the macroscopic response.

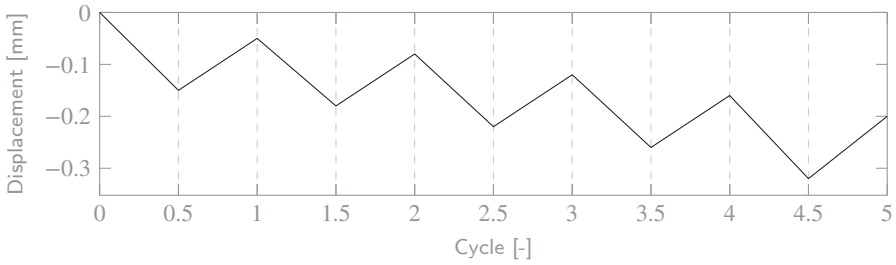


**Figure 20:** Imposed displacement path for the compressive cyclic loading.

loops while the model without closure can not. In order to analyze the resources of this phenomenon, we marked the macroscopic stiffness of the material in Fig. 22. The macroscopic plastic deformation and the degree of loss of stiffness are quantified in Table. 3. The degree of damage along the cycles is represented by an equivalent variable $d_i$. The expression gives as (Roubin, 2013):

$$d_i = \frac{E_0^{\mathrm{M}} - E_i^{\mathrm{M}}}{E_0^{\mathrm{M}}}, \tag{27}$$

where $E_i^{\mathrm{M}}$ represents the macroscopic elastic module at $i^{\mathrm{th}}$ cycle and $E_0^{\mathrm{M}}$ represents the one at initial stage.

For the stiffness of the material, it can be seen from Fig. 22 and Table. 3 that the model without closure losses much more stiffness during the cycles. The equivalent damage variable is also more significant than the other model. This is because the model with closure has its stiffness partially recovers by the crack closures. Meanwhile, the crack closures dissipate a lot more energy, which clearly corresponds to the area of the hysteresis loops at the macro-scale.

For the macroscopic plastic deformation observed in the material's responses, it can be seen that the model with closure shows higher increasing values of plasticity over the cycles. It is worth noting that no plasticity mechanism is formulated directly in the model at the local scale. The observed plasticity at the macro-scale is related to the residual sliding-opening remaining in a large number of elements, which is also related to the dissipated energy during friction. The sliding closing mechanism allows the model to dissipate more energy along with the cycles, resulting in a greater amount of residual sliding opening.

Finally, let us take a look at the evolution of the number of localized/closing elements, see Fig. 23. We can see that the majority of localization takes place during the first cycle. It means that during the later four cycles, sliding

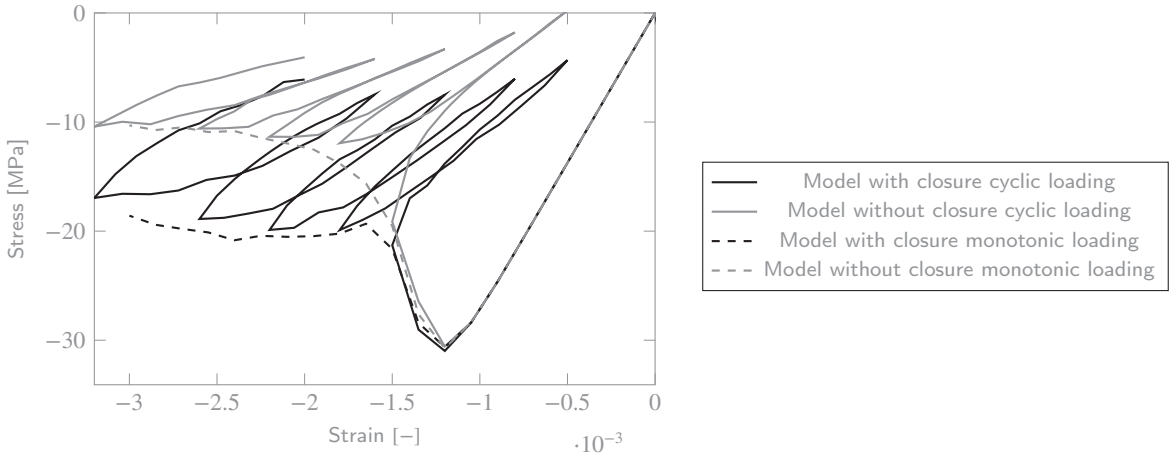


**Figure 21:** Macroscopic responses of the model with and without closure under compressive cyclic loadings.

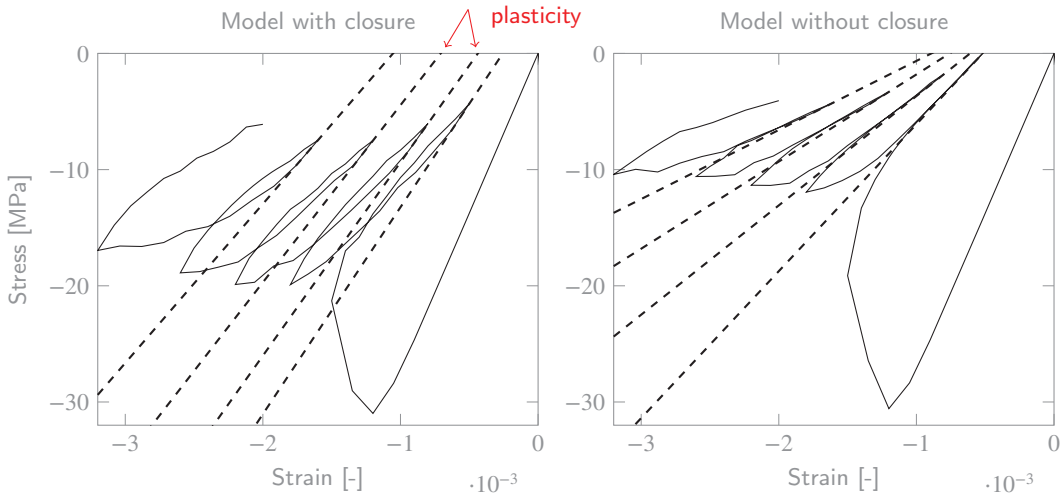


**Figure 22:** Illustration of the macroscopic stiffness and the plasticity in cyclic loading for the model with/without closures.

opening/closing and re-opening/re-closing behaviors mainly occur in the same groups of elements. As expected, the two models present a similar increasing rate for the number of localized elements since they have the same localization criterion. The figure also shows that the number of closing elements decreases and increases as the cyclic displacement loads and unloads, but a number of elements always remain in the closing status. Among several reasons for this observation, the most important one is that the degree of damage is different for each localized element, and the most damaged elements are the easiest to trigger the closure process. Thus, a number of elements admit a closing process during the first unloading phase. Then in the subsequent reloading phases, only a group of elements reaches the maximum sliding opening value and switches to the open state, while other elements are still in the closing state. It is very likely that the sliding opening/closing and re-opening/re-closing behaviors are mainly performed in a group of most vulnerable elements.

## 6. Numerical modeling and comparison with experimental results

In this section, the performance of the developed model is tested by comparing it to experimental results. The experimental data is provided by Piotrowska (2013), in which, experimental characterizations of concrete behaviors are well detailed. To establish the effect of the granular skeleton, three types of aggregates are used. The objective of

**Table 3**
Variation of the degree of damage and the macroscopic plasticity during cycles, the model exhibits crack closure mechanism is marked in red.

| Cycle $i$ | Macroscopic elastic module $E_i^M$ [GPa] | | Damage $d_i$ [-] | | Macroscopic plastic deformation $\varepsilon_i^p$ $[10^{-3}]$ | |
|---|---|---|---|---|---|---|
| 0 | 27.5 | 27.5 | 0 | 0 | 0 | 0 |
| 1 | 17.8 | 12.6 | 0.35 | 0.54 | 0.26 | 0.52 |
| 2 | 16.7 | 9.4 | 0.39 | 0.66 | 0.44 | 0.61 |
| 3 | 15.3 | 7.5 | 0.44 | 0.73 | 0.71 | 0.76 |
| 4 | 13.7 | 5.9 | 0.50 | 0.79 | 1.05 | 0.89 |

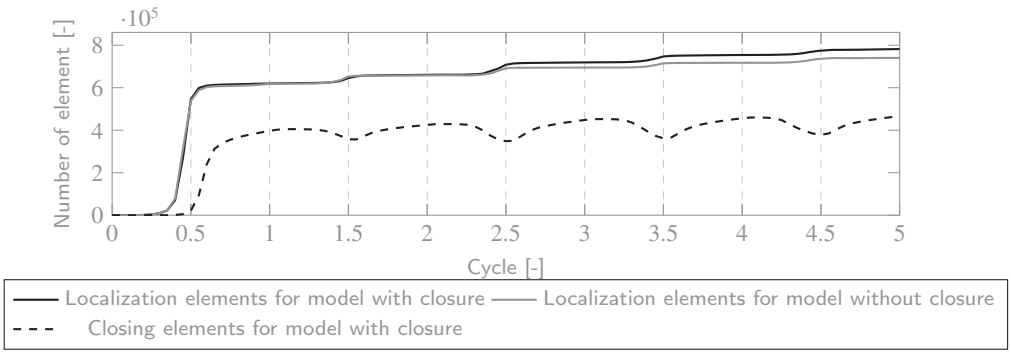


**Figure 23:** Accumulate number of localized elements and closing elements along the 5 cycles for the model with/without closure.

this section is to provide a reasonable comparison between the numerical simulation and the experimental results.

It is worth noting that in the following section, regarding some limitations of our numerical model, several simplifications are applied to the numerical simulations:

- The resolution of the E-FEM model is static. The rate of loading is not taken into account.
- The boundary conditions used in numerical simulations are not the same as in experimental tests. Indeed, there is friction between the concrete sample and the cap in contact with the sample, but we are not able to simulate this kind of contact. In the following numerical simulations, it is considered that the upper and lower surfaces of the sample have a free displacement in the lateral direction, *i.e.* no friction is considered.
- There are macropores in the cement matrix of the concrete, but we have no further information on their percentage. Therefore, the macropores are not simulated in our model.
- Temperature, humidity, and maturity of the concrete are considered as influencing factors, and their effects are reflected in the material parameters.

This section contains three parts. First, the morphological models are constructed according to the formulations of samples and the type of aggregates. Second, the identification of material parameters is presented. In the third part, the constructed models are applied to monotonic/cyclic compression tests and are compared to experimental results. Some details and analysis of the numerical simulation are addressed in this part.

## 6.1. Construction of the mesoscopic morphological models

### *6.1.1. Preparation of the specimens in experiments (Piotrowska, 2013)*

The studied specimen is cylindric with 7 centimeters in diameter and 14 centimeters in height. The length/diameter ratio is equal to 2, which enables the specimen to be tested under high confinement pressure, and prevents the samples from buckling by limiting the influence of boundary conditions. The study provides investigations on three different concretes, which are distinguished by the type of aggregate:

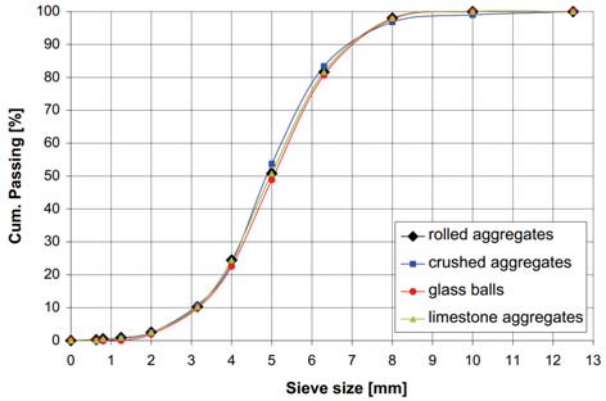


**Figure 24:** Granulometry curves of coarse aggregates used in the studied concretes (Piotrowska, 2013).

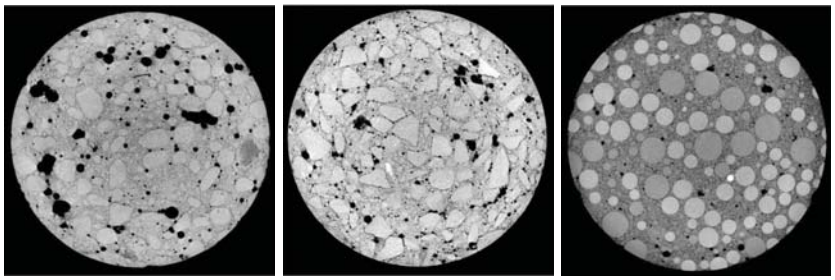

(a) Rolled aggregate concrete (b) Crushed aggregate concrete (c) Glass ball concrete

**Figure 25:** Tomographic cross-sectional view of three concretes varying by aggregate types (Piotrowska, 2013).

- rolled aggregate concrete (SR): rolled siliceous aggregates derived from a natural deposit;
- crushed aggregate concrete (SC): crushed aggregates obtained from the siliceous rock;
- glass ball concrete (GB): glass balls.

Except for the type of aggregates, concretes have the same cement matrix and the same aggregate volume fraction to minimize variables. The distributions of the size of aggregates are arranged as similar as possible, see Fig. 24. The fabrication of the specimens is to cast the concrete into a 13.5-liter parallelepiped mold; after 28 days of conservation, the block is then cored and grounded into a cylinder shape. Therefore, part of aggregates in the concretes will be cut. It can be seen in the X-ray tomographic images Fig. 25.

### *6.1.2. Construct morphological models using packing spheres*

The first step of the numerical construction consists in generating the morphological structure. The used method is formulated in Stamati, Andò, Roubin, Cailletaud, Wiebicke, Pinzon, Couture, Hurley, Caulk, Caillerie et al. (2020). The key point is to arrange $N$ spheres of ranging size and place them randomly in the field while ensuring that there is no overlap between them . Hence we have a set of spheres $b(r_i, d_i)$, with $r_i$ represents the coordinate of the center of the sphere, and $d_i$ the diameter. In a ranging size of spheres, the distribution of diameters is nearly linear.

The construction of the numerical model with spheres fits well with the GB (glass ball) concrete. However, we are not able to generate complex shape articles in the field yet. Hence, the morphological structures of SR (rolled aggregate) concrete and SC (crushed aggregate) concrete are also constructed using spheres. Different critical parameters of the interface are used to represent the differences between coarse aggregates. We take the GB concrete as an example to represent the construction of the morphological model.

According to provided information by Piotrowska (Piotrowska, 2013), the volume fraction of the aggregates is 40%, which is chosen to be the same for three concretes. The diameter of glass balls varies from 1.5 millimeters

**Table 4**
Six classes that are used to generate morphological heterogeneities in GB concrete to reproduce the granulometry as in experiments.

| Category | Diameter ranging [mm] | Relative percentage | Volume fraction |
|---|---|---|---|
| 1 | [1.5, 2.5] | 5% | 2% |
| 2 | [2.5, 4] | 17% | 6.8% |
| 3 | [4, 5] | 27% | 10.8% |
| 4 | [5, 6] | 26% | 10.4% |
| 5 | [6, 7.5] | 20% | 8% |
| 6 | [7.5, 9] | 5% | 2% |

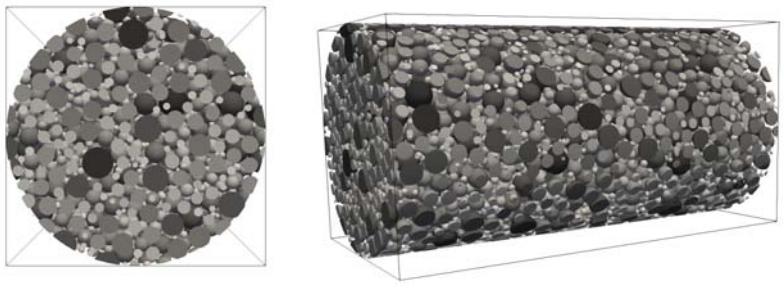

(a) Axial view of the defined field (b) 3D view of the defined field

**Figure 26:** Generated field which is defined by six classes, aiming at representing the morphological heterogeneities of GB concrete.

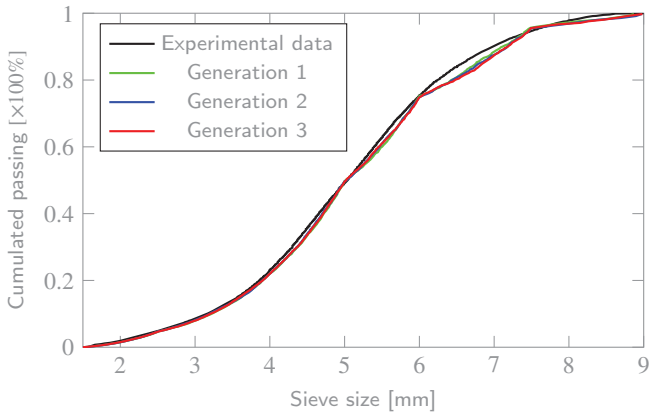


**Figure 27:** Comparison of the GB concrete granulometry between the provided experimental data and generated fields.

to 9 millimeters, and the size of glass balls respect the granulometry shown in Fig. 24. In order to reconstruct the morphological heterogeneities in concrete with the same size distribution, the range of aggregates is divided into six classes, see Table. 4.

The generated cylindric field is shown in Fig. 26. Different colors distinguish the spheres of the six classes. As it is mentioned previously, we can see that spheres are scattered randomly in the field, and there is no overlap between them.

We generated three different fields by using the same setting (Table. 4). The measured distribution of these generated fields is given in Fig. 27. It can be seen that there is no obvious difference between these three generated fields and the experimental data. It declares that we can practically rebuild a sufficiently similar morphological heterogeneities

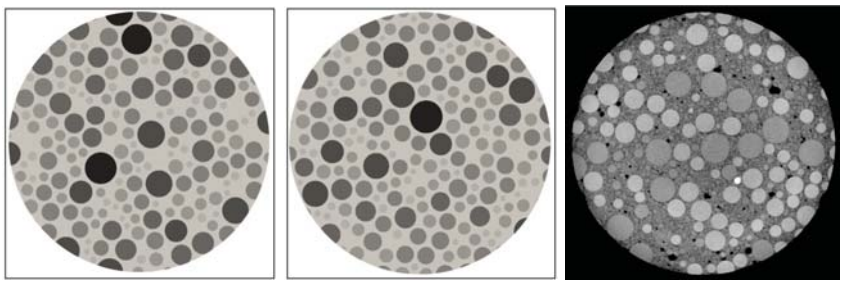

(a) Section view of a random morphology (b) Section view of another random morphology (c) Tomographical X-ray image

**Figure 28:** Comparison between two generations and the tomographic X-ray image for GB concrete.

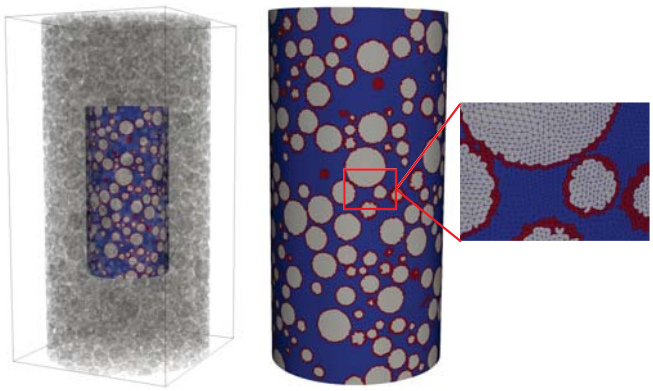

(a) Defined field with random morphology (b) Projection to an unstructured mesh

**Figure 29:** Projection of the defined field for GB concrete onto an unstructured Finite Element mesh.

of the concrete. It can also be verified in section views, see Fig. 28.

It is worth noting that in this paper, the choice is made to have only one weak discontinuity embedded in a finite element. Hence, a finite element can only correctly present morphological information if there is at most one heterogeneous interface passing through the element. However, the small diameters of the spheres and the narrowness between inclusions result in the need for fine meshes, which increases the computing time and required memory to an incredible level.

To build a morphological model that exhibits consistent geometry information as the experimental specimen, and can be calculated with feasible required memory and computing time, the choice is made here to construct a model in the center of the cylindrical sample with half diameter and half height. As shown in Fig. 29, the projection produces three types of elements, corresponding to the matrix, aggregates, and weakly enhanced elements. In the zoom figure Fig. 29(b), it can be seen that the weakly enhanced elements of one inclusion do not overlap with the weakly enhanced elements of another inclusion, which means that each weakly enhanced element contains only one weak discontinuity. This morphological model carries 1.2 million nodes. The required calculating memory is around 7 GB.

The choice of establishing a morphological model of semi-cylinder leads to several inconsistencies with the experimental specimen. For example, it is hard to ensure the volume fraction of the semi-cylinder. In order to illustrate the effect of the specimen size, we propose here an example by using the same cube as present in section 5.

We generate 5 fields using the same setting as the cube in section 5, each of them is then cut into cubes with different lengths, 80 mm, 60 mm, and 40 mm. In order to eliminate other influencing factors, the same mesh and material parameters are used for all these cubes. The average macroscopic responses of the cube of different sizes are

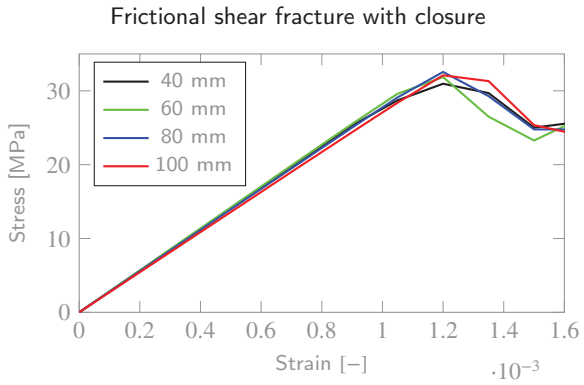


**Figure 30:** Average macroscopic responses of 5 realizations of the cube of different sizes.

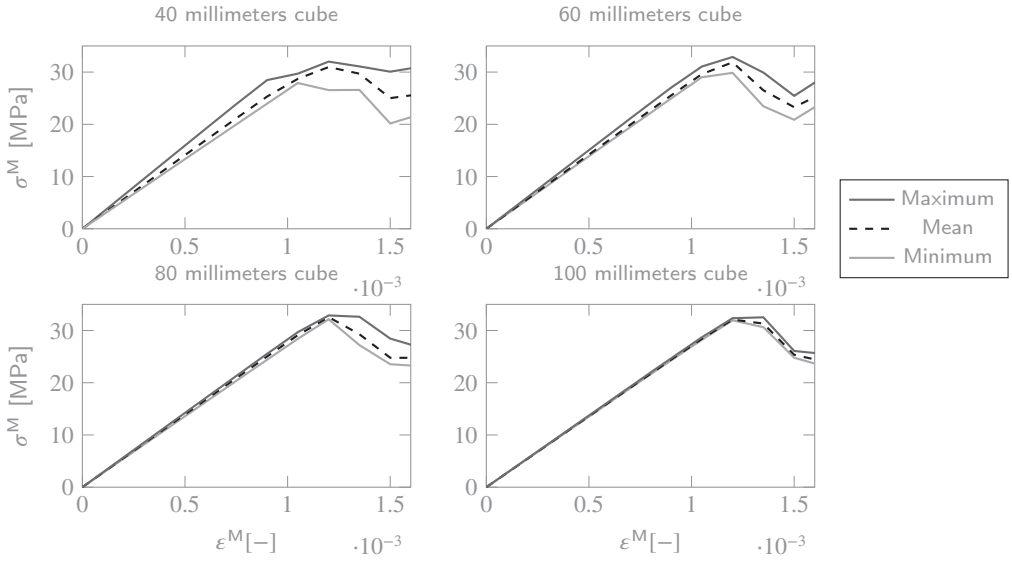


**Figure 31:** Illustration of the effect of the specimen size.

plotted in Fig. 30. It can be seen from the figure that the average macroscopic responses of the cube with different sizes are very similar.

Then our interest is made on the diversification of the cube's responses of different sizes. In Fig. 31, the minimum and the maximum macroscopic response values of the cubes are plotted together with the average values. It can be seen that the smallest cube shows the most significant diversification, with the largest difference between the minimum and maximum curves. This is because the small cube carries a low ratio between the size of the cube and that of the aggregates, which results in greater uncertainty in the aspect of the volume fraction and the morphological structure.

This result indicates that the morphological model of the semi-cylinder is capable of providing mechanical behaviors that are comparable with the experimental results. In order to avoid falling into particular cases, three different fields are generated for each type of concrete.

## 6.2. Identification of material parameters

This section aims at finding the correct parameters for the material to reproduce the observed experimental responses of the concrete. The experimental responses of concretes are plotted in Fig. 32.

As it is mentioned previously, three kinds of concrete are considered: the rolled siliceous (SR) concrete, the crushed siliceous (SC) concrete, and the glass ball (GB) concrete. Among them, the aggregate of the type siliceous is the same for SR and SC concrete. The properties of the aggregates are summarized in Table. 5. As we can see, the aggregate contains a much higher compressive strength compared with the concrete. Therefore, for the sake of simplification,

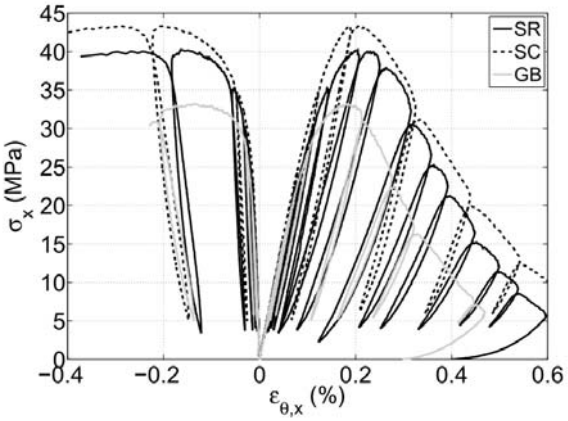


**Figure 32:** Experimental macroscopic responses of concretes in compressive loadings (Piotrowska, 2013).

we consider that the aggregates have a pure elastic behavior, *i.e.* no crack occurs in the aggregate elements.

**Table 5**
Identified material characteristics of inclusions in compressive tests (Piotrowska, 2013).

| Aggregate type | Siliceous | Glass |
|---|---|---|
| Young's modulus $E$ [GPa] | 78 | 70 |
| Poisson's ratio $\nu$ [-] | 0.12 | 0.22 |
| Macroscopic compressive strength $\sigma_c^{\mathrm{M}}$ [MPa] | 330 | $\approx 1000$ |

In summary, for each type of concrete, eight unknown parameters are required to be identified to reproduce the observed responses in experiments, see Table. 6. It is worth noting that the matrix is the same for each kind of concrete. Hence, the matrix' parameter $E_1$, $\nu_1$, $C_1$, $\varphi_1$, and $\mathcal{G}_{\mathrm{op}1}$ should be the same for all three types of concrete.

The unknown parameters are identified by comparing the simulation results with the experimental ones in simple compressive loading. Among the unknown parameters, Young's module $E_1$ and the Poisson's ratio $\nu_1$ can be determined in the elastic phase. The work of Hashin and Shtrikman (1963) allows us to determine an upper and lower limit for the modulus of elasticity. Then the other unknown parameters are referred to as the failure parameters, which are related to the failure behaviors of the concrete in the macro-scale.

The cohesion $C$, the fracture energy $\mathcal{G}_{\mathrm{op}}$, and the friction angle $\varphi$ are parameters that are related to the failure behaviors of the material. For the same value of the fracture energy $\mathcal{G}_{\mathrm{op}}$, a larger cohesion $C$ produces a higher macroscopic strength and a more fragile behavior of the material at the softening stage. For the same value of cohesion $C$, a larger fracture energy $\mathcal{G}_{\mathrm{op}}$ leads to a more ductile behavior at the softening stage and a higher resistance. The friction angle $\varphi$ influences only the resistance of the material and has no effect on the softening behavior. This is due to the fact that the traction-separation laws (sliding-opening and sliding-closing law) that govern the behaviors of the material after localization are independent with the friction angle.

After the identification, the obtained parameters for all three types of concretes are listed in Table. 7. It is worth noting that for each kind of concrete, a set of three different random morphological structures is considered. Clearly, another set of three random microstructures would lead to different material parameters since the size of this statistical sampling is not large enough to reduce the numerical discrepancy.

Table. 7 shows that three concretes carry identical parameters for the matrix. As for the weakly enhanced elements, the SC concrete with the most coarse aggregates carries the largest value of the cohesion, the fracture energy, and the friction angle. The GB concrete, on the contrary, is the smallest. This fact provides a good agreement with the physical definitions of these parameters. After the material parameters are identified, cyclic loadings are applied to the material. The comparison between the numerical simulations and the experimental results are plotted in Fig. 35.

**Table 6**
The known (black) and unknown (blue) parameters.

| | $E$ [GPa] | $\nu$ [-] | $C$ [MPa] | $tan\varphi$ [-] | $\mathcal{G}_{\mathsf{op}}$ $[J/m^2]$ |
|---|---|---|---|---|---|
| Matrix | $E_1$ | $\nu_1$ | $C_1$ | $tan\varphi_1$ | $\mathcal{G}_{\mathsf{op1}}$ |
| Interface | $E_1$ & $E_2$ | $\nu_1$ & $\nu_2$ | $C_2$ | $tan\varphi_2$ | $\mathcal{G}_{\mathsf{op2}}$ |
| Siliceous aggregate | $E_2 = 78$ | $\nu_2 = 0.12$ | - | - | - |
| Glass aggregate | $E_2 = 70$ | $\nu_2 = 0.22$ | - | - | - |

**Table 7**
Identified parameters for three different types of concrete.

| Concrete | $E$ [GPa] | $\nu$ [-] | $C$ [MPa] | $tan\varphi$ [-] | $\mathcal{G}_{\mathsf{op}}[J/m^2]$ |
|---|---|---|---|---|---|
| Matrix | 11.5 | 0.16 | 14.0 | 0.46 | 2.8 |
| Siliceous aggregates for SC & SR concrete | 78.0 | 0.12 | - | - | - |
| Glass aggregates for GB concrete | 70.0 | 0.22 | - | - | - |
| Interface for SC concrete | - | - | 12.0 | 0.46 | 2.5 |
| Interface for SR concrete | - | - | 12.0 | 0.20 | 2.5 |
| Interface for GB concrete | - | - | 6.0 | 0.167 | 0.4 |

## 6.3. Comparison between the numerical simulation and the experimental results

The material's parameters for three different concretes have been defined in the previous section. In this part, the cyclic loadings are applied to the material with the same parameters. For each concrete, the trajectory of the imposed displacement is determined by the provided experimental data.

This section consists of three parts. We present in the first part the evolution of the crack patterns in concretes, especially the influences of the crack closure mechanism. Thus the attention is focused on the comparison between a same specimen in different loading steps. Here, we take the SC concrete in monotonic compressive loading as an example. In the second part, our interest is made on a comparison between different concretes. Finally, the performances of the model at the macro-scale are discussed.

In order to present what happened inside the material during the compressive loading, we take two loading stages of the SC concrete as examples: at the macroscopic strain equal to 0.4 and 0.6. Crack patterns are drawn in Fig. 33. The evolution of the sliding-opening values and the closing values are illustrated in the figure. It can be seen from Fig. 33 that a large group of elements is localized in the material, many of which have a very small sliding opening value (1.0e-04 mm). In many cases, these slightly opened elements can be considered as ignorable. The failure behaviors of the material are mainly governed by macro-cracks.

As we have introduced previously, the more damaged elements are more vulnerable and have the priority to continue to open. Hence, rather than creating new major cracks, the material tends to enlarge already exist major cracks. This can be verified in Fig. 33(a) and Fig. 33(b) that the major cracks become deeper and more localized. Referring to the crack closures, we can see in Fig. 33(c) that the closing elements are gathered beside the macro-cracks. They are triggered by the stress release caused by the fast propagation of the macro-cracks.

Second, in order to present the influences of the type of aggregates, we present a comparison between the SC concrete and the GB concrete, which are the concretes containing the coarsest and the smoothest aggregates. Regarding the parameters of the material for three different types of concrete, it can be seen from Table. 7 that the SC concrete has the largest values for failure parameters while the GB concrete has the smallest ones. Here, the same loading stage is chosen at the strain is equal to 0.48.

The crack patterns for the two concrete are shown in Fig. 34. It is worth noting that they have different morphological features, thus the cracks will initiate and propagate in different positions. Despite this difference, it can be seen that the multi-crack feature for SC concrete has more branches. The GB concrete has fewer macro-cracks, but the cracks are more "localized" and "concentrated". These observations correspond to a more fragile behavior of the GB concrete and verify the physical meanings of our material parameters.

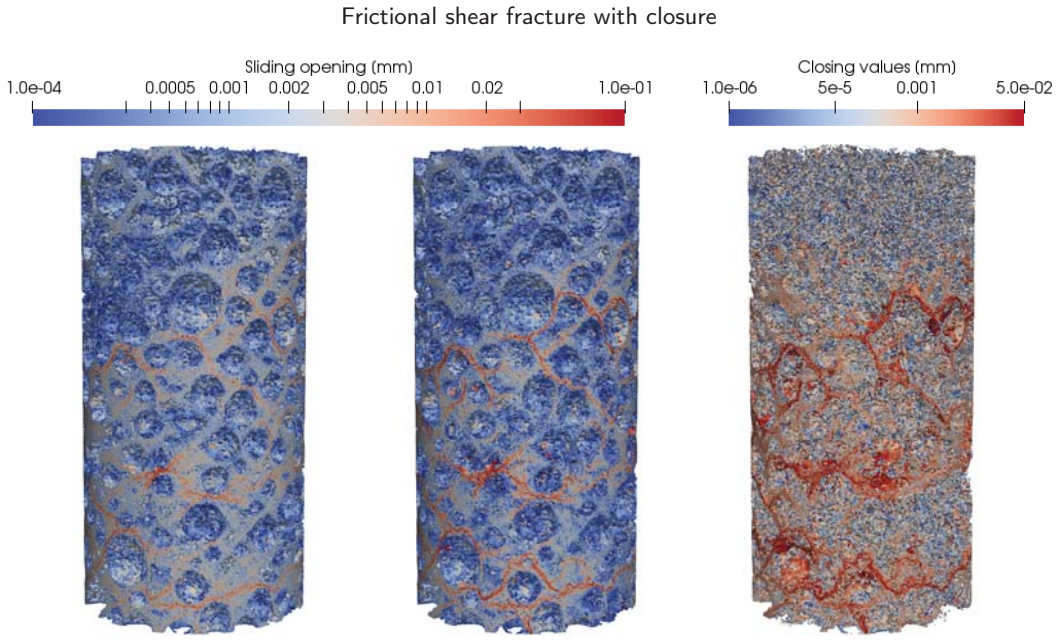


(a) Sliding opening values at the macroscopic strain equals to 0.4 (b) Sliding opening values at the macroscopic strain equals to 0.6 (c) Closing values at the macroscopic strain equals to 0.6

**Figure 33:** Crack pattern in SC concrete at different loading stage, with (a) and (b) present the sliding opening values, and (c) present the closing values.

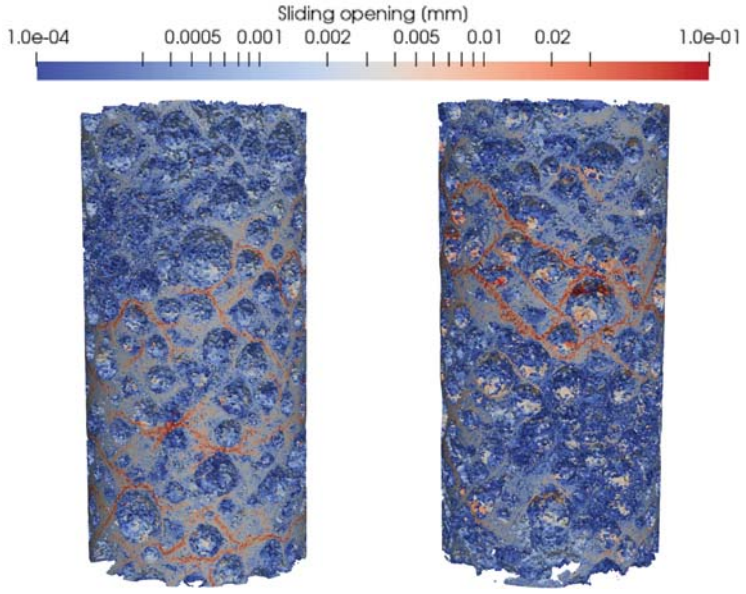


(a) SC concrete (b) GB concrete

**Figure 34:** Crack pattern for SC concrete and GB concrete at the same macroscopic strain which equals to 0.48.

Finally, our attention is focused on the behaviors of the model at the macro-scale, see Fig. 35. Before going into details of the analysis, it is noted here that though the required memory for calculation is constant, the needed solving time will increase as the loading proceeds, because there are more elements carrying strong discontinuities and expecting non-linear solutions at the element level. Aiming at reducing total computation time, the choice is made

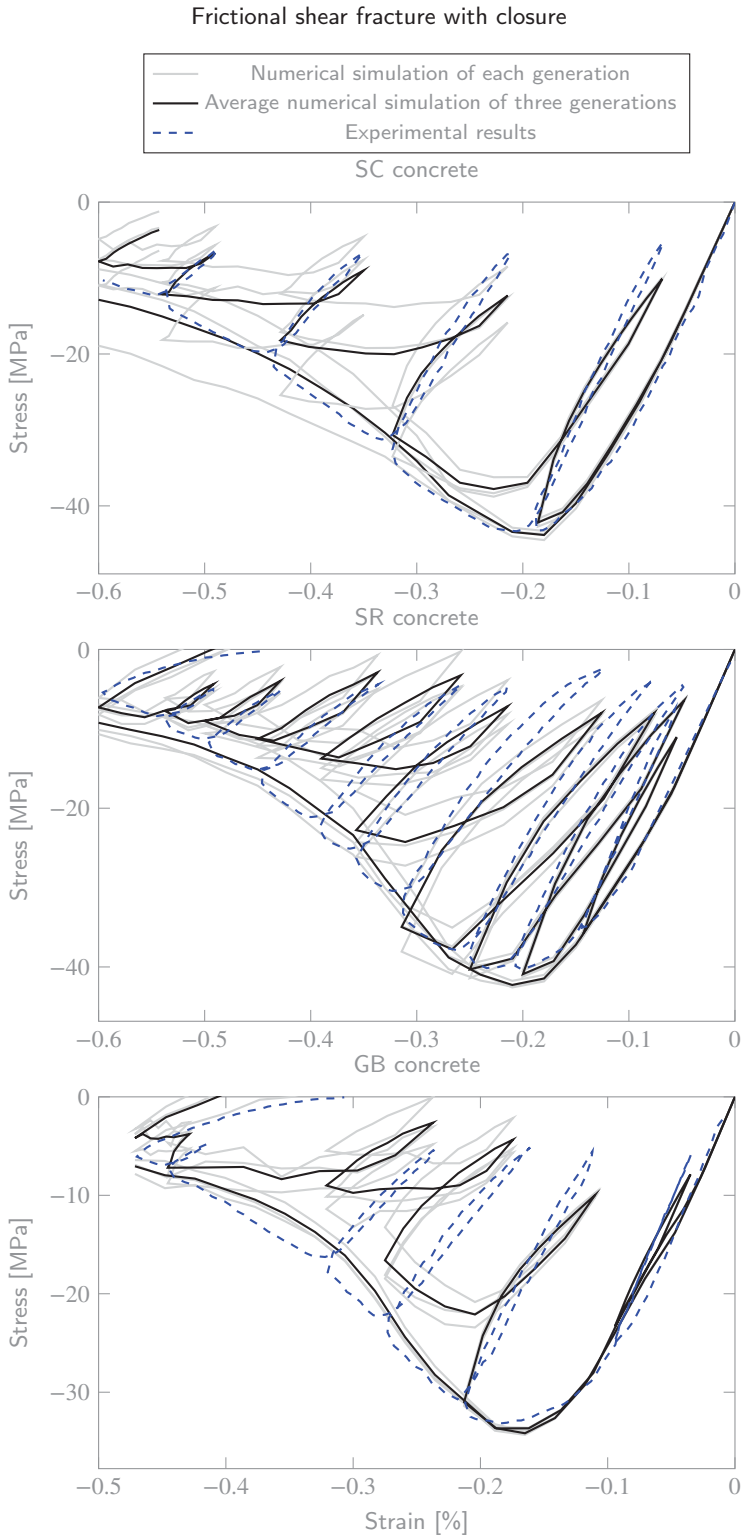


**Figure 35:** Comparison between the experimental results and the numerical simulations for SC, SR and GB concretes.

here to impose the lowest possible time steps for each cycle. The choice to produce only three realizations for each type of concrete is also made based on the limitation of calculation resources.

Fig. 35 shows the macroscopic responses of three generations of each concrete along with their average values. In simple compressive loadings, it can be seen that despite some diversity between the three different realizations, the average responses of the material show good consistency with the experimental results, with the same elastic module, resistance, and softening failure behavior. As for the compressive cyclic loadings, the hysteresis phenomenon is also well attained. However, it can also be noticed that the decreasing of the material's strength and hysteresis loops is faster than the experimental results, especially after several cycles. This observed phenomenon is related to one of the assumption in this study that the erosion of the roughness between micro-cracks is permanent and irreversible. This hypothesis implies that the friction will fate quickly after a few cycles. Without new appeared cracks, the friction in existing cracks will tend to zero after several cycles.

## 7. Conclusions and discussions

This paper is designed to describe and model various failure behaviors of quasi-brittle materials such as concrete, especially the behaviors under compressive cyclic loadings. In the present study, it is assumed that the complex behaviors in macro-scale take their origin at smaller scales, and are strongly related to the heterogeneous structure of the material. Upon consideration, the used method is the Enhanced Finite Element Method (E-FEM), which enables the discontinuity kinematics in the formulation. Targeted at the compressive behaviors of the material, the strong discontinuity of the type mode-II is chosen in this study to simulate the frictional shear fractures between the lips of cracks. Two mechanisms is added to the model:

- We add in the model a closing mechanism, which enables the model to simulate the crack sliding forward (opening) and backward (closing),
- We add in the model the weak discontinuity which is independent and additive to the mode-II strong discontinuity. Hence the effect of the heterogeneity interface can be taken into concern.

The performance of the model is illustrated by applying it to a concrete-like specimen. From local scale to macroscopic scale, complex mechanical behaviors can be observed:

- First, in simple monotonic loadings, the asymmetric responses in tension/compression can be noticed. Yet, the model is not adapted to be applied to tensile loadings, the compressive to tensile strength ratio is rather low.
- Second, the crack closure mechanism can be observed in monotonic loadings, that the opening of a macro-crack will lead to a set of meso-cracks to close, and result in a deeper and thinner crack pattern.
- Finally, the hysteresis phenomena can be obtained in cyclic loadings, such as the progressive loss of stiffness, the macroscopic plastic deformation, and hysteresis loops. By comparing it with the model without closure, it is demonstrated that the closing mechanism is an essential ingredient for the hysteresis phenomena.

The model is then tested by comparing it with experimental results. In the work of Piotrowska (2013), three kinds of concretes are constructed with the same cement paste and different types of aggregates. We managed at constructing the same heterogeneity structure as the experiments with the same volume fraction and granulometry distribution. The material parameters are identified by comparing with experimental results. As a result, the numerical simulation shows a good agreement in comparing with the experimental results at the macro-scale. Furthermore, the material parameters demonstrate a good consistency with their physical meanings.

Yet, the hypothesis of the irreversible and permanent erosion of the friction between micro-cracks leads to a result that the model has higher rate in losing material strength and decreasing hysteresis loops. Considering this weak point, the model could be further improved by imposing a long-lasting friction between micro-cracks. The numerical simulation is also limited by the computational capacity, especially for a calculation with a large number of time steps such as cyclic loadings. We can improve the performance of the model by speeding up the calculation, which will enable us to produce more realizations for a material and make the prediction of material behavior more accurate.

## Appendix A - Explicit expressions of the interpolation matrix

We present the explicit expressions of the interpolation matrix in Eq. (12) and Eq. (13) in this part. Readers can refer to Roubin et al. (2015) for details of development.

- $\mathbf{G}_{\mathrm{w}}$ is the interpolation matrix for the weak discontinuity:

$$\mathbf{G}_{\mathrm{w}} = \begin{cases} \mathbf{G}_{\mathrm{w}}^{+} = \Theta^{+}\boldsymbol{H}_{\mathrm{w}} = \frac{V^{-}}{V}\boldsymbol{H}_{\mathrm{w}} & \text{in } \Omega_e^{+} \\ \mathbf{G}_{\mathrm{w}}^{-} = \Theta^{-}\boldsymbol{H}_{\mathrm{w}} = -\frac{V^{+}}{V}\boldsymbol{H}_{\mathrm{w}} & \text{in } \Omega_e^{-}, \end{cases}$$

- $\mathbf{G}_{\mathrm{s}}$ is the interpolation matrix for the actual field corresponding to the strong discontinuity:

$$\mathbf{G}_{\mathrm{s}} = (\bullet \otimes \nabla\varphi_e)^{s},$$

with $\varphi_e$ is a explicitly defined arbitrary function to separate nodes at $\Omega_e^{+}$ from $\Omega_e^{-}$ by setting unit value to nodes at $\Omega_e^{+}$ and null at other part. The arbitrary function is defined as:

$$\varphi_e(\boldsymbol{x}) = \sum_{a=1}^{n_{\mathrm{e}}} \boldsymbol{N}_a p_a \text{ with } p_a = \begin{cases} 1 & \text{if node number } a \in \Omega_e^{+} \\ 0 & \text{if node number } a \in \Omega_e^{-}. \end{cases}$$

- $\mathbf{G}_{\mathrm{s}}^{*}$ is the interpolation matrix for the virtual field corresponding to the strong discontinuity, which contains a bounded part and an unbounded part, $\mathbf{G}_{\mathrm{s}}^{*} := \mathbf{G}_{\mathrm{s,b}}^{*} + \mathbf{G}_{\mathrm{s,u}}^{*}$:

$$\begin{cases} \mathbf{G}_{\mathrm{s,b}}^{*} = -\frac{A}{V}\boldsymbol{H}_{\mathrm{s}}^{*}, \\ \mathbf{G}_{\mathrm{s,u}}^{*} = \delta_{\mathcal{S}}\boldsymbol{H}_{\mathrm{s}}^{*}, \end{cases}$$

where the term $\boldsymbol{H}_{\mathrm{s}}^{*}$ is equal to $(\bullet \otimes \boldsymbol{n})^{\mathrm{sym}}$, and carries only the information of the normal vector $\boldsymbol{n}$.

## Appendix B - Explicit expressions of the modified stiffness matrix $K$

We present in this part the expression of the stiffness matrix $K$ in Eq. (17) and Eq. (18):

$$\begin{aligned}
\boldsymbol{K}_{\mathrm{bb}} &= \boldsymbol{B}^{T}\left(V^{+}\boldsymbol{C}^{+} + V^{-}\boldsymbol{C}^{-}\right)\boldsymbol{B} \\
\boldsymbol{K}_{\mathrm{bw}} &= \frac{V^{+}V^{-}}{V}\boldsymbol{B}^{T}(\boldsymbol{C}^{+} - \boldsymbol{C}^{-})\boldsymbol{H}_{\mathrm{w}} \\
\boldsymbol{K}_{\mathrm{bs}} &= \boldsymbol{B}^{T}(V^{+}\boldsymbol{C}^{+} + V^{-}\boldsymbol{C}^{-})\mathbf{G}_{\mathrm{s}}\boldsymbol{n}_p \\
\boldsymbol{K}_{\mathrm{wb}} &= \frac{V^{+}V^{-}}{V}\boldsymbol{H}_{\mathrm{w}}{}^{T}(\boldsymbol{C}^{+} - \boldsymbol{C}^{-})\boldsymbol{B} \\
\boldsymbol{K}_{\mathrm{ww}} &= \frac{V^{+}V^{-}}{V}\boldsymbol{H}_{\mathrm{w}}{}^{T}(V^{-}\boldsymbol{C}^{+} + V^{+}\boldsymbol{C}^{-})\boldsymbol{H}_{\mathrm{w}} \\
\boldsymbol{K}_{\mathrm{ws}} &= \frac{V^{+}V^{-}}{V}\boldsymbol{H}_{\mathrm{w}}(\boldsymbol{C}^{+} - \boldsymbol{C}^{-})\mathbf{G}_{\mathrm{s}}\boldsymbol{n}_p. \\
\boldsymbol{K}_{\mathrm{s^*b}} &= (\boldsymbol{n}_t + \boldsymbol{n}\tan\varphi)\frac{1}{V}\boldsymbol{H}_{\mathrm{s}}^{*,T}(V^{+}\boldsymbol{C}^{+} + V^{-}\boldsymbol{C}^{-})\boldsymbol{B} \\
\boldsymbol{K}_{\mathrm{s^*w}} &= (\boldsymbol{n}_t + \boldsymbol{n}\tan\varphi)\frac{V^{+}V^{-}}{V}\boldsymbol{H}_{\mathrm{s}}^{*,T}(\boldsymbol{C}^{+} - \boldsymbol{C}^{-})\boldsymbol{H}_{\mathrm{w}} \\
\boldsymbol{K}_{\mathrm{s^*s}} &= (\boldsymbol{n}_t + \boldsymbol{n}\tan\varphi)\frac{1}{V}\boldsymbol{H}_{\mathrm{s}}^{*,T}(V^{+}\boldsymbol{C}^{+} + V^{-}\boldsymbol{C}^{-})\boldsymbol{G}_{s}\boldsymbol{n}_p \\
K_{\mathrm{qo}} &= \frac{C^2}{\mathcal{G}_{\mathrm{op}}}e^{-C[u]/\mathcal{G}_{\mathrm{op}}}
\end{aligned}$$

## References

Alliche, A., 2004. Damage model for fatigue loading of concrete. International Journal of Fatigue 26, 915–921.

Bažant, Z.P., Jirásek, M., 2002. Nonlocal integral formulations of plasticity and damage: survey of progress. Journal of Engineering Mechanics 128, 1119–1149.

Belytschko, T., Moës, N., Usui, S., Parimi, C., 2001. Arbitrary discontinuities in finite elements. International Journal for Numerical Methods in Engineering 50, 993–1013.

Benkemoun, N., Hautefeuille, M., Colliat, J., Ibrahimbegovic, A., . Heterogeneous materials failure: 3d meso-scale modeling with embedded discontinuities .

Benkemoun, N., Hautefeuille, M., Colliat, J.B., Ibrahimbegovic, A., 2010. Failure of heterogeneous materials: 3d meso-scale fe models with embedded discontinuities. International journal for numerical methods in engineering 82, 1671–1688.

Chen, A.C., Chen, W.F., 1975. Constitutive relations for concrete. Journal of Engineering Mechanics 101.

Comi, C., Perego, U., 2001. Fracture energy based bi-dissipative damage model for concrete. International Journal of Solids and Structures 38, 6427–6454. URL: http://linkinghub.elsevier.com/retrieve/pii/S002076830100066X, doi:10.1016/S0020-7683(01)00066-X.

Corless, R.M., Gonnet, G.H., Hare, D.E., Jeffrey, D.J., Knuth, D.E., 1996. On the lambertw function. Advances in Computational mathematics 5, 329–359.

Dias-da Costa, D., Alfaiate, J., Sluys, L., Júlio, E., 2009a. A discrete strong discontinuity approach. Engineering Fracture Mechanics 76, 1176–1201.

Dias-da Costa, D., Alfaiate, J., Sluys, L., Júlio, E., 2009b. Towards a generalization of a discrete strong discontinuity approach. Computer Methods in Applied Mechanics and Engineering 198, 3670–3681.

Desmorat, R., Ragueneau, F., Pham, H., 2007. Continuum damage mechanics for hysteresis and fatigue of quasi-brittle materials and structures. International Journal for Numerical and Analytical Methods in Geomechanics 31, 307–329. URL: http://doi.wiley.com/10.1002/nag.532, doi:10.1002/nag.532.

Dolbow, J., Moës, N., Belytschko, T., 2000. Discontinuous enrichment in finite elements with a partition of unity method. Finite elements in analysis and design 36, 235–260.

Dragon, A., Mroz, Z., 1979. A continuum model for plastic-brittle behaviour of rock and concrete. International Journal of Engineering Science 17, 121–137.

Dvorkin, E.N., Cuitiño, A.M., Gioia, G., 1990. Finite elements with displacement interpolated embedded localization lines insensitive to mesh size and distortions. International journal for numerical methods in engineering 30, 541–564.

Hashin, Z., Shtrikman, S., 1963. A variational approach to the theory of the elastic behaviour of multiphase materials. Journal of the Mechanics and Physics of Solids 11, 127–140.

Hauseux, P., 2015. Propagation d'incertitudes paramétriques dans les modèles numériques en mécanique non linéaire: applications à des problèmes d'excavation. Ph.D. thesis. Lille 1.

Hauseux, P., Roubin, E., Seyedi, D.M., Colliat, J.B., 2016. Fe modelling with strong discontinuities for 3d tensile and shear fractures: application to underground excavation. Computer Methods in Applied Mechanics and Engineering 309, 269–287.

Hofstetter, G., Mang, H., 1995. Computational mechanics of reinforced concrete structures. Vieweg+ Teubner Verlag.

Ibrahimbegović, A., Gharzeddine, F., Chorfi, L., 1998. Classical plasticity and viscoplasticity models reformulated: theoretical basis and numerical implementation. International journal for numerical methods in engineering 42, 1499–1535.

Ibrahimbegovic, A., Markovic, D., Matthies, H.G., Niekamp, R., Taylor, R.L., 2005. Multi-scale modelling of heterogeneous structures with inelastic constitutive behavior, in: Complas VIII-8th International Conference on Computational Plasticity, Citeseer.

Jebli, M., Jamin, F., Malachanne, E., Garcia-Diaz, E., El Youssoufi, M.S., 2018. Experimental characterization of mechanical properties of the cement-aggregate interface in concrete. Construction and Building Materials 161, 16–25.

Jirasek, Zimmermann, T., 1998. Analysis of rotating crack model (1998a) .

Kupfer, H., Hilsdorf, H.K., Rusch, H., 1969. Behavior of Concrete Under Biaxial Stresses. ACI Journal Proceedings 66, 656–666. URL: http://www.concrete.org/Publications/ACIMaterialsJournal/ACIJournalSearch.aspx?m=details{&}ID=7388, doi:10.14359/7388.

Lemaitre, J., Chaboche, J.L., Benallal, A., Desmorat, R., 2009. Mécanique des matériaux solides-3eme édition. Dunod.

Mariani, S., Perego, U., 2003. Extended finite element method for quasi-brittle fracture. International Journal for Numerical Methods in Engineering 58, 103–126.

Matthies, H., Strang, G., 1979. The solution of nonlinear finite element equations. International journal for numerical methods in engineering 14, 1613–1626.

Mazars, J., 1984. Application de la mécanique de l'endommagement au comportement non linéaire et à la rupture du béton de structure. THESE DE DOCTEUR ES SCIENCES PRESENTEE A L'UNIVERSITE PIERRE ET MARIE CURIE-PARIS 6 .

Mihai, I.C., Jefferson, A.D., 2011. A material model for cementitious composite materials with an exterior point eshelby microcrack initiation criterion. International Journal of Solids and Structures 48, 3312–3325.

Moës, N., Cloirec, M., Cartraud, P., Remacle, J.F., 2003. A computational approach to handle complex microstructure geometries. Computer methods in applied mechanics and engineering 192, 3163–3177.

Moës, N., Dolbow, J., Belytschko, T., 1999. A finite element method for crack growth without remeshing. International journal for numerical methods in engineering 46, 131–150.

Oliver, J., 1996a. Modelling strong discontinuities in solid mechanics via strain softening constitutive equations. part 1: Fundamentals. International journal for numerical methods in engineering 39, 3575–3600.

Oliver, J., 1996b. Modelling strong discontinuities in solid mechanics via strain softening constitutive equations. part 2: Numerical simulation. International journal for numerical methods in engineering 39, 3575–3600.

Oliver, J., 2000. On the discrete constitutive models induced by strong discontinuity kinematics and continuum constitutive equations. International Journal of Solids and Structures 37, 7207–7229. URL: www.elsevier.com/locate/ijsolstr, doi:10.1016/S0020-7683(00)00196-7.

Oliver, J., Huespe, A.E., Sánchez, P.J., 2006. A comparative study on finite elements for capturing strong discontinuities: E-FEM vs X-FEM. Computer Methods in Applied Mechanics and Engineering 195, 4732–4752. URL: www.elsevier.com/locate/cma, doi:10.1016/j.cma.

2005.09.020.
Ortiz, M., Leroy, Y., Needleman, A., 1987. A finite element method for localized failure analysis. Computer methods in applied mechanics and engineering 61, 189–214.
Pandolfi, A., Krysl, P., Ortiz, M., 1999. Finite element simulation of ring expansion and fragmentation: the capturing of length and time scales through cohesive models of fracture. International Journal of Fracture 95, 279–297.
Peerlings, R., De Borst, R., Brekelmans, W., Geers, M., 1998. Gradient-enhanced damage modelling of concrete fracture. Mechanics of Cohesive-frictional Materials: An International Journal on Experiments, Modelling and Computation of Materials and Structures 3, 323–342.
Pijaudier-Cabot, G., Bažant, Z.P., 1987. Nonlocal damage theory. Journal of engineering mechanics 113, 1512–1533.
Piotrowska, E., 2013. Rôle du squelette granulaire dans le comportement du béton sous trés fortes contraintes: analyse expérimentale et numérique. Ph.D. thesis. Université de Grenoble.
Ragueneau, F., 2007. Comportements endommageants des matériaux et des structures en béton armé. LMT-Cachan.
Ramakrishnan, V., Malhotra, T.B.V., 1993. Fatigue strength and endurance limit of lightweight concrete. Special Publication 136, 397–420.
Rots, J.G., Nauta, P., Kuster, G., Blaauwendraad, J., 1985. Smeared crack approach and fracture localization in concrete. HERON, 30 (1), 1985 .
Roubin, E., 2013. Modélisation EF et morphologique de milieu hétérogènes à l'échelle mésoscopique: applications aux matériaux à matrices cimentaire. Ph.D. thesis. Thèse de doctorat, Ecole Normale Supérieure de Cachan.
Roubin, E., Stamati, O., Ando, E., Malecot, Y., 2019. FE mesoscopic modelling of a micro-concrete based on x-ray scanmorphologies, in: FraMCoS-X : Fracture Mechanics of Concrete and Concrete Structures, Bayonne, France. URL: https://hal.univ-grenoble-alpes.fr/hal-02057978.
Roubin, E., Vallade, A., Benkemoun, N., Colliat, J.B., 2015. Multi-scale failure of heterogeneous materials: A double kinematics enhancement for embedded finite element method. International Journal of Solids and Structures 52, 180–196.
Salençon, J., 2002. De l'élasto-plasticité au calcul à la rupture. Editions Ecole Polytechnique.
Scrivener, K.L., Crumbie, A.K., Laugesen, P., 2004. The interfacial transition zone (itz) between cement paste and aggregate in concrete. Interface science 12, 411–421.
Simo, J., Oliver, J., 1994. A new approach to the analysis and simulation of strain softening in solids. Fracture and damage in quasibrittle structures , 25–39.
Simo, J.C., Oliver, J., Armero, F., 1993. An analysis of strong discontinuities induced by strain-softening in rate-independent inelastic solids. Computational mechanics 12, 277–296.
Simo, J.C., Rifai, M.S., 1990. A class of mixed assumed strain methods and the method of incompatible modes. International Journal for Numerical Methods in Engineering 29, 1595–1638. URL: http://doi.wiley.com/10.1002/nme.1620290802, doi:10.1002/nme.1620290802.
Stamati, O., Andò, E., Roubin, E., Cailletaud, R., Wiebicke, M., Pinzon, G., Couture, C., Hurley, R.C., Caulk, R., Caillerie, D., et al., 2020. spam: Software for practical analysis of materials. Journal of Open Source Software 5, 2286.
Sukumar, N., Chopp, D.L., Moës, N., Belytschko, T., 2001. Modeling holes and inclusions by level sets in the extended finite-element method. Computer methods in applied mechanics and engineering 190, 6183–6200.
Taylor, R.L., 1987. FEAP-ein finite element analysis programm. Ing.-Gemeinschaft Klee & Wrigges.
T.C. Hsu, T., 1981. Fatigue of plain concrete. Journal of the American Concrete Institute 78, 292–305.
Vallade, A., 2016. Modélisation multi-échelles des shales: influence de la microstructure sur les propriétés macroscopiques et le processus de fracturation. Ph.D. thesis. Lille 1.
Washizu, K., 1968. Variational methods in elasticity and plasticity. Google Scholar .
Wells, G.N., 2001. Discontinuous modelling of strain localisation and failure. Ph.D. thesis.
Wells, G.N., Sluys, L., 2001. A new method for modelling cohesive cracks using finite elements. International Journal for Numerical Methods in Engineering 50, 2667–2682.
Wells, G.N., Sluys, L.J., 2000. Three-dimensional embedded discontinuity model for brittle fracture. Technical Report 5. URL: www.elsevier.com/locate/ijsolstr, doi:10.1016/S0020-7683(00)00029-9.
Wilson, E.L., 1974. The static condensation algorithm. International Journal for Numerical Methods in Engineering 8, 198–203.
Wosatko, A., Genikomsou, A., Pamin, J., Polak, M.A., Winnicki, A., 2018. Examination of two regularized damage-plasticity models for concrete with regard to crack closing. Engineering Fracture Mechanics 194, 190–211.
Yang, D., Dong, W., Liu, X., Yi, S., He, X., 2018. Investigation on mode-i crack propagation in concrete using bond-based peridynamics with a new damage model. Engineering Fracture Mechanics 199, 567–581.